Journal of Computational Acoustics, Vol. 15, No. 3 (2007) 285–318

INTERNATIONAL ASSOCIATION
FOR MATHEMATICS AND
COMPUTERS IN SIMULATION

ACCURATE TREATMENT OF A GENERAL SLOPING INTERFACE IN A FINITE-ELEMENT 3D NARROW-ANGLE PE MODEL

FRÉDÉRIC STURM

Laboratoire de Mécanique des Fluides et d'Acoustique
UMR CNRS 5509, École Centrale de Lyon
36 Avenue Guy de Collongue
FR-69 134 Ecully Cedex, France
frederic.sturm@ec-lyon.fr

NIKOLAOS A. KAMPANIS

Institute of Applied and Computational Mathematics
F.O.R.T.H., 71110 Heraklion, Greece
kampanis@iacm.forth.gr

Received 12 December 2005
Accepted 18 October 2006

Parabolic equation models in 3D usually apply the "staircase" approximation to general range–varying interfaces between adjacent layers. This is the simplest technique available: it consists in neglecting range and azimuthal derivatives in the associated interface conditions. Our aim in this paper is to analyze the influence of the stair-step approximation technique, common to most 3D PE models, on a one-way sound wave propagation problem. We present a new finite-element 3D narrow-angle PE model which accurately treats the variable interface conditions. This is accomplished by using (i) an appropriate parabolized condition of the same aperture as the parabolic equation used, and (ii) a new change-of-variable technique which does not require any homotheticity condition of the layers as in previous works. Numerical simulations for the 3D wedge problem are presented. The convergence of the numerical solutions with respect to the azimuth is investigated. Unlike other 3D PE models working in cylindrical coordinates, the convergence tests have been carried out using a range-dependent number of points in azimuth. Numerical solutions obtained with the newly developed model are compared with a reference solution based on the image source and with a solution obtained with a 3D PE model that uses a stair-step technique.

Keywords: Acoustic models; three-dimensional parabolic equation; change-of-variable technique.

1. Introduction

Parabolic equation (PE) based models are largely used by the underwater acoustics community since they simulate efficiently sound propagation problems in complex oceanic environments.[1] Parabolic equation models in two dimensions (2D PE) assume that the environment is symmetric with respect to the azimuth. This assumption allows the azimuthal derivative terms to be dropped wherever they appear, i.e. in the governing parabolic equation and in the sloping bottom (or interface) conditions. The acoustic field in this case is computed in the range/depth (vertical) plane, using a marching scheme to advance in range, and a finite element or finite difference approximation in depth. In oceanic environments where refraction due to sound speed and bathymetry changes with respect to the azimuth is indeed weak, the 3D acoustic field may be computed by several independent calculations along adjacent, vertical planes utilizing 2D PE models; the environmental parameters used in each 2D calculation correspond to those of the 3D environment sampled at the corresponding azimuth.[2] The resulting model is referred to as an N×2D (or pseudo 3D) model and the underlying assumption is that coupling of energy from one azimuth to another can be disregarded. However, there are many examples of oceanic waveguides where the horizontal refraction of energy is significant in some areas[3–5] and the N×2D approximation does not model propagation correctly. A full 3D model is therefore needed.

Among the existing three-dimensional models,[6] 3D PE codes have been developed in order to model the azimuthal coupling of energy.[7–15] They have been used to compute propagation in a number of three-dimensional environments and to show acoustical effects not predicted by any 2D model. However, the bottom slopes (both in range and azimuth) are generally handled using a stair-step approximation, i.e. the 3D varying bathymetry is replaced in each azimuth by a sequence of stair-steps. The bottom geometry is hence assumed to be locally horizontal though it is allowed to vary in depth at each range step in a marching algorithm. Sloping bottom conditions are often replaced accordingly by flat bottom conditions, hence neglecting the range- and azimuthal-components in boundary (or interface) conditions.[a] Neglecting the range component in the normal derivative condition at the water-sediment interface can lead to non-energy-conserving 2D PE models. This well-known problem has been extensively studied by many authors (see for instance in Ref. 16) and efficient solutions have been proposed to overcome this problem in some two-dimensional environments.[17–24]

For the 3D case, studies were conducted in the hope of showing that neglecting the azimuthal component in transmission conditions may affect the horizontal refraction of energy. In Ref. 25, the standard narrow-angle three-dimensional parabolic equation was rewritten in a new coordinate system in order to handle properly the varying bottom topography, eliminating the need for a stair-step approximation. However, using this change-of-variable technique leads to numerical models that require a lot of memory and can lead to very large CPU times in comparison with other 3D PE codes that use the staircase approximation. Indeed, after the transformation of the coordinate system, the initial- and boundary-value problem is slightly more complicated, with additional lower-order terms in the partial differential equation and range- and azimuth-varying coefficients. As a consequence, it is not possible to split the resulting operator into a depth and azimuthal operator as in other approaches. Instead, a large system of linear equations in depth and azimuth is obtained at each step in range. These linear systems are sparse and their inversion requires the use of iterative algorithms. Due to memory storage limitations, the use of any direct

[a]Notice that the only term that accounts for azimuthal coupling in such 3D PE models is the partial differential derivative with respect to the azimuth present in the underlying parabolic equation.

algorithm (such as Gaussian elimination) becomes impossible. Besides the above-mentioned transformation technique, an important feature of the numerical model of Ref. 25 was that the classical boundary conditions had been previously parabolized tightly following the paraxial approximation made on the Helmholtz equation, and incorporated into the finite element discretization. This step revealed itself to be essential to obtain a mathematically well-posed initial- and boundary-value problem and correct energy properties. The method was implemented in a numerical code named TRIPARADIM and numerical solutions were compared with other numerical solutions calculated by the three-dimensional PE code of Ref. 9, which approximates the water-sediment interface as locally horizontal stair steps.[26,27] The test case chosen was a 3D extension of the ASA 2D wedge benchmark.[28] Satisfactorily, the two different 3D PE methods predicted qualitatively the same three-dimensional effects. However, some quantitative differences were noticed between the two 3D solutions: for each modal initialization, a shift in the phasing was observed (this shift being more pronounced for large ranges) and the amplitudes were in rather good agreement except for lower energies (corresponding to shadow-zone regions).

It should be noted that in both codes, for numerical and computation purposes, the physical propagation domain (which consisted of a water layer overlying a lossy homogeneous halfspace sedimental layer) had been truncated in depth and an artificial absorbing layer with a depth-dependent attenuation coefficient had been added. In TRIPARADIM, the transformation of the physical domain into a simpler one was performed using an affine mapping so that each interface separating two adjacent layers became flat in the mapped computation domain. The change-of-variable technique required each layer to be homothetical, thus imposing to consider a non-horizontal artificial absorbing layer with a range- and azimuth-varying width in the physical domain. This assumption was not required by the 3D PE code of Ref. 9, for which the absorbing layer was horizontal and had a constant width. Due to memory storage limitations, the artificial layer used in TRIPARADIM was not thick enough to properly attenuate sound propagation inside the bottom, causing reflections on the lower boundary, and leading to the presence of spurious energy in the shadow zone region. Besides, recent numerical simulations using another more flexible code[15,29] have shown that the 3D computations performed with TRIPARADIM were carried out using an undersampled depth grid (but with a correct number of points in the azimuthal direction). Indeed, though a meticulous convergence test was in the process of being performed (which consisted in running the model several times using various range, azimuthal, and depth increments with decreasing values until stabilization of the numerical solution), the computations had to be stopped because the memory limitation of the computer had been reached. Note that a uniform mesh length was used in depth; a correct description of the acoustic field necessitated a large number of grid points, most of which were located in the artificial absorbing layer. Undersampling by a factor of 2 in depth can change the numerical solution by at least the same order of magnitude as the differences between the two 3D PE solutions shown in Refs. 26 and 27. Therefore, the differences (in both phase and amplitude) observed in Refs. 26 and 27 cannot be unambiguously attributed to the stair-step approximation technique.

In this paper, we re-examine the importance of carefully handling the azimuthal component in the sloping bottom conditions when processing computations using 3D PE models. For this purpose, we develop a new 3D narrow-angle PE model that treats the interface scattering very accurately without assuming any homotheticity condition on each layer of the varying waveguide. As in Ref. 25, we treat the exact normal derivative interface condition using a parabolized approximation consistent with the narrow-angle paraxial approximation made on the Helmholtz equation. The energy-conserving, 3D narrow-angle PE model is recalled in Sec. 2. The numerical treatment of irregular, variable bottoms topography is done via an appropriate change of variable which maps the physical domain into a cylindrical computational domain. The change-of-variable technique avoids the stair-step approximation of the bottom. It is given in Sec. 3. Its main advantage is that it does not require any homotheticity condition of the layers. The transformed initial- and boundary-value problem in the mapped computation domain is presented in Sec. 3. An energy-conserving weak formulation is derived and exact energy properties of the model are established. In Sec. 4, the application of a finite-element discretization scheme is illustrated. In order to gain more in flexibility, we consider a mesh not necessarily uniform in depth. This allows us to reduce the number of points in both the sedimental and artificial absorbing layers. In the proposed scheme, a large linear system with a block-tridiagonal structure is required to be solved at each step in range, in contrast to several smaller diagonal systems required in any splitting technique based method.[8–10,14,15] We solve these linear systems using a non-stationary iterative algorithm equivalent to the preconditioned conjugate gradient iteration method for the normal equation. The algorithm is given explicitly. In Sec. 5, numerical results for the 3D wedge problem are discussed and it is shown that the use of the iterative algorithm proves to be very satisfying except when propagating in the nearfield. Grid convergence of the numerical solutions is investigated. Unlike other 3D PE models working in cylindrical coordinates, the convergence tests have been carried out using a range-dependent number of points in the azimuthal direction. At each step in range, the number of points used in azimuth has been selected such that the corresponding arclength increment remain less than a given fraction of the acoustical wavelength. Comparisons with a reference solution based on the image source and with numerical solutions obtained running a 3D PE model that uses stair-step technique are shown. In the concluding section the advantages and drawbacks of the proposed numerical model are summarized and forthcoming improvements are discussed.

2. The Energy-Conserving, 3D, Narrow-Angle PE Model

We consider a waveguide consisting in a fluid water layer of constant density ρ_{w}, attenuation $\alpha_{\mathrm{w}}^{(\lambda)}$, and sound speed c_{w}, and a fluid sediment layer of constant density ρ_{s}, attenuation $\alpha_{\mathrm{s}}^{(\lambda)}$ and sound speed c_{s}, overlying an absorbing (artificial) bottom layer of finite depth to simulate a fluid bottom halfspace of constant density ρ_{a}, increasing (with depth) attenuation $\alpha_{\mathrm{a}}^{(\lambda)}$ and constant sound speed c_{a}. The topography of the waveguide and the artificial bottom varies in 3D in general. Hence, the water-sediment interface Σ_{sed} is allowed to vary in 3D.

We assume that the interface Σ_{abs} separating the sediment layer from the absorbing layer, is horizontal. The problem is formulated in cylindrical coordinates, with z denoting the depth (increasing downwards) below the sea surface, θ the azimuthal (bearing) angle, and r the horizontal range from the source. Let $0 < s(r,\theta) < z_{\text{abs}} < z_{\max}$ for $r \geq 0$, $0 \leq \theta \leq 2\pi$, where $\{z = s(r,\theta)\}$ is the water-sediment interface Σ_{sed}, $\{z = z_{\text{abs}}\}$ is the sediment-bottom interface Σ_{abs}, and $z_{\max}$ is the maximum depth of the absorbing layer. We consider a time-harmonic point source emitting at frequency f and placed at the origin at depth $z = z_S$. In the frequency domain, the acoustic pressure field $P = P(r,\theta,z)$ satisfy the 3D Helmholtz equation:

$$\rho\left[\frac{1}{r}\frac{\partial}{\partial r}\left(\frac{r}{\rho}\frac{\partial P}{\partial r}\right) + \frac{\partial}{\partial z}\left(\frac{1}{\rho}\frac{\partial P}{\partial z}\right) + \frac{1}{r^2}\frac{\partial}{\partial \theta}\left(\frac{1}{\rho}\frac{\partial P}{\partial \theta}\right)\right] + k_\alpha^2 P = -\frac{2}{r}\,\delta(r)\delta(z - z_S), \tag{1}$$

for $r \geq 0$, $\theta \in [0, 2\pi]$, $z \in (0, s(r,\theta)) \cup (s(r,\theta), z_{\text{abs}}) \cup (z_{\text{abs}}, z_{\max})$, where $k_\alpha = k(1 + \mathrm{i}\eta\alpha^{(\lambda)})$ is the complex-valued wavenumber, with $k = 2\pi f/c$ and c the sound speed, $\alpha^{(\lambda)}$ the attenuation expressed in decibels per wavelength, $\eta = 1/(40\pi \log_{10} \mathrm{e})$ (with $\eta\alpha^{(\lambda)} \ll 1$), and ρ the density. We assume that c, $\alpha^{(\lambda)}$ and ρ are defined by their restrictions on each fluid layer. For instance, $\rho = \rho_{\text{w}}$ if $z \in (0, s(r,\theta))$, $\rho = \rho_{\text{s}}$ if $z \in (s(r,\theta), z_{\text{abs}})$, and $\rho = \rho_{\text{a}}$ if $z \in (z_{\text{abs}}, z_{\max})$. Besides, we assume that c, $\alpha^{(\lambda)}$ and ρ are smooth functions for $r \geq 0$, $0 \leq \theta \leq 2\pi$, $z \in (0, s(r,\theta)) \cup (s(r,\theta), z_{\text{abs}}) \cup (z_{\text{abs}}, z_{\max})$, with possible jump discontinuities across the interfaces $\{z = s(r,\theta)\}$ and $\{z = z_{\text{abs}}\}$. The acoustic pressure P is assumed to satisfy a pressure-release boundary condition $P = 0$ at $\{z = 0\}$ and $\{z = z_{\max}\}$, an outgoing radiation condition in r, and a 2π-periodic condition in azimuth $P|_{\theta=0} = P|_{\theta=2\pi}$. The pressure P on $\{z = s(r,\theta)\}$ satisfies the following transmission conditions:

$$P(r,\theta,s^-(r,\theta)) = P(r,\theta,s^+(r,\theta)), \qquad r \geq 0, \quad \theta \in [0,2\pi], \tag{2}$$

$$\frac{1}{\rho_{\text{w}}}\frac{\partial P}{\partial \eta}(r,\theta,s^-(r,\theta)) = \frac{1}{\rho_{\text{s}}}\frac{\partial P}{\partial \eta}(r,\theta,s^+(r,\theta)), \quad r \geq 0, \quad \theta \in [0,2\pi]. \tag{3}$$

Here, the superscript notations "+" and "−" signify above and below the Σ_{sed} interface respectively, and the operator $\partial/\partial\eta$ is the normal derivative defined by:

$$\frac{\partial}{\partial \eta} = \frac{\partial}{\partial z} - (\partial_r s)\frac{\partial}{\partial r} - \frac{1}{r^2}(\partial_\theta s)\frac{\partial}{\partial \theta}. \tag{4}$$

The pressure P also satisfies the following transmission conditions at $\{z = z_{\text{abs}}\}$:

$$P(r,\theta,z_{\text{abs}}^-) = P(r,\theta,z_{\text{abs}}^+), \qquad r \geq 0, \quad \theta \in [0,2\pi],$$

$$\frac{1}{\rho_{\text{s}}}\frac{\partial P}{\partial z}(r,\theta,z_{\text{abs}}^-) = \frac{1}{\rho_{\text{a}}}\frac{\partial P}{\partial z}(r,\theta,z_{\text{abs}}^+), \qquad r \geq 0, \quad \theta \in [0,2\pi].$$

For the derivation of parabolic equations (PE), we introduce a reference sound speed c_0 and a reference real-valued wavenumber $k_0 = 2\pi f/c_0$. As we are mainly interested in outgoing component of the propagating field, we factor the pressure as $P(r,\theta,z) = H_0^1(k_0 r)v(r,\theta,z)$

where H_0^1 denotes the zeroth-order Hankel function of the first kind. we use the asymptotic development:

$$H_0^1(k_0 r) \approx \sqrt{\frac{2}{\pi k_0 r}} \mathrm{e}^{\mathrm{i}(k_0 r - \pi/4)}, \quad k_0 r \to +\infty. \tag{5}$$

Let $r_{\max} > 0$. We assume a weak dependence of the medium characteristics with respect to the range and that the backscattering energy is neglectable. Moreover, assuming that r^{-2} approximately commutes with $\partial/\partial r$ for $r \gg 0$, Eq. (1) is factored out and, under the assumption of a slowly varying medium and for narrow angles of propagation with respect to the horizontal radial direction, a Taylor series expansion of the resulting square-root operator is used, yielding the following parabolic equation:

$$\frac{\partial v}{\partial r} = \frac{\mathrm{i}\rho}{2k_0}\left[\frac{\partial}{\partial z}\left(\frac{1}{\rho}\frac{\partial v}{\partial z}\right) + \frac{1}{r^2}\frac{\partial}{\partial \theta}\left(\frac{1}{\rho}\frac{\partial v}{\partial \theta}\right)\right] + \frac{\mathrm{i}k_0}{2}\beta v, \tag{6}$$

for $r \in [0, r_{\max}]$, $\theta \in [0, 2\pi]$, and $z \in (0, s(r,\theta)) \cup (s(r,\theta), z_{\mathrm{abs}}) \cup (z_{\mathrm{abs}}, z_{\max})$, where $\beta(r,\theta,z) = (c_0(1 + \mathrm{i}\eta\alpha^{(\lambda)})/c(r,\theta,z))^2 - 1$. By simplifying by ρ (since ρ is constant on each layer), Eq. (6) is the standard PE of Tappert[30] which was first used for 3D computations by Baer.[7] The 3D PE given by Eq. (6) has narrow-angle capabilities both in depth and in azimuth. Other 3D PE models handle wide-angle capability in depth.[8–15,29,31] The acoustic field v is assumed to satisfy the following initial condition at $r = 0$:

$$v(0,\theta,z) = v^0(\theta,z), \qquad \theta \in [0,2\pi], \quad z \in [0, z_{\max}], \tag{7}$$

where v^0 denotes an initial outgoing field simulating a point-source at $r = 0$ and $z = z_S$, pressure-release boundary conditions at $\{z = 0\}$ and $\{z = z_{\max}\}$:

$$v(r,\theta,0) = v(r,\theta,z_{\max}) = 0, \qquad r \in [0, r_{\max}], \quad \theta \in [0,2\pi], \tag{8}$$

and a 2π-periodic condition in azimuth:

$$v(r,0,z) = v(r,2\pi,z), \qquad r \in [0,r_{\max}], \quad z \in [0,z_{\max}]. \tag{9}$$

The transmission condition (2) for the pressure field P at $\{z = s(r,\theta)\}$ leads to the continuity condition for v:

$$v(r,\theta,s^-(r,\theta)) = v(r,\theta,s^+(r,\theta)), \qquad r \in [0,r_{\max}], \quad \theta \in [0,2\pi]. \tag{10}$$

The transmission condition for v obtained from the transmission condition (3) for the pressure P at $\{z = s(r,\theta)\}$, is replaced by the "parabolized" approximate transmission condition given by:

$$\frac{1}{\rho_{\mathrm{w}}}\frac{\partial v}{\partial T}(r,\theta,s^-(r,\theta)) = \frac{1}{\rho_{\mathrm{s}}}\frac{\partial v}{\partial T}(r,\theta,s^+(r,\theta)), \qquad r \in [0,r_{\max}], \quad \theta \in [0,2\pi], \tag{11}$$

where the operator $\partial/\partial T$ is defined by:

$$\frac{\partial}{\partial T} = \frac{\partial}{\partial z} - \mathrm{i}k_0(\partial_r s)\mathcal{I} - \frac{1}{r^2}(\partial_\theta s)\frac{\partial}{\partial \theta}. \tag{12}$$

The parabolized operator given by Eq. (12) represents a generalization to 3D problems of the 2D parabolized normal condition used by Abrahamsson and Kreiss[32] to construct a stable 2D PE-based marching algorithm for a range-dependent duct (composed of one single layer). It has been derived considering on the range-component of the normal derivative (4) the following horizontal plane wave impedance approximation:

$$\frac{\partial P}{\partial r} \approx \mathrm{i}k_0 P. \tag{13}$$

It can be shown that this horizontal plane wave approximation has been implicitly used as an underlying approximation in the derivation of Eq. (6), i.e. in the linear paraxial approximation of the Helmholtz equation. The reader is referred to Ref. 33 for more details. It should be noted that in any 3D PE model that uses a stair-step approximation and accordingly assumes the bottom geometry as locally horizontal, the transmission condition for v obtained from the transmission condition (3) for the pressure P at $\{z = s(r,\theta)\}$, is replaced by the following "flat bottom" transmission condition:

$$\frac{1}{\rho_{\mathrm{w}}}\frac{\partial v}{\partial z}(r,\theta,s^-(r,\theta)) = \frac{1}{\rho_{\mathrm{s}}}\frac{\partial v}{\partial z}(r,\theta,s^+(r,\theta)), \qquad r \in [0, r_{\max}], \quad \theta \in [0, 2\pi], \tag{14}$$

where the range- and azimuthal-components in the "parabolized" interface condition (11) have been neglected.

The acoustic field v satisfies at $\{z = z_{\mathrm{abs}}\}$ the following transmission conditions:

$$v(r,\theta,z^-_{\mathrm{abs}}) = v(r,\theta,z^+_{\mathrm{abs}}), \qquad r \in [0, r_{\max}], \quad \theta \in [0, 2\pi], \tag{15}$$

$$\frac{1}{\rho_{\mathrm{s}}}\frac{\partial v}{\partial z}(r,\theta,z^-_{\mathrm{abs}}) = \frac{1}{\rho_{\mathrm{a}}}\frac{\partial v}{\partial z}(r,\theta,z^+_{\mathrm{abs}}), \qquad r \in [0, r_{\max}], \quad \theta \in [0, 2\pi]. \tag{16}$$

Following the notations used by Dougalis *et al.* in Ref. 34, the parabolized condition given by Eq. (11) leads to the $\|\cdot\|_\rho$-stability condition:

$$\frac{\mathrm{d}}{\mathrm{d}r}\left(\int_0^{2\pi}\int_0^{z_{\max}} |v(r,\theta,z)|^2 \,\frac{\mathrm{d}z\,\mathrm{d}\theta}{\rho}\right) \leq 0, \tag{17}$$

for $0 < r \leq r_{\max}$. Equation (17) holds as an equality (i.e., the model is $\|\cdot\|_\rho$-conserving) if the attenuation coefficient is null. The energy estimate (17) can be established by multiplying (6) by $\rho^{-1}\bar{v}$ where $\bar{v}$ denotes the complex conjugate of v, integrating by parts using (11), and taking real parts. Equation (17) is a stability condition which ensures the existence and uniqueness of a solution to the 3D PE (6) supplied with the transmission and boundary conditions (7)–(11), (15), (16). It generalizes the stability condition derived by Dougalis *et al.* in Ref. 34 for the analog 2D range-independent problem in a multilayered waveguide.

Notice that the normal derivative condition for v obtained from (3) and using (5), can be written:

$$\frac{1}{\rho_{\mathrm{w}}}\left[\frac{\partial v}{\partial z} - \partial_r s\left(\left(\mathrm{i}k_0 - \frac{1}{2r}\right)v + \frac{\partial v}{\partial r}\right) - \frac{\partial_\theta s}{r^2}\frac{\partial v}{\partial \theta}\right](r,\theta,s^-(r,\theta))$$
$$= \frac{1}{\rho_{\mathrm{s}}}\left[\frac{\partial v}{\partial z} - \partial_r s\left(\left(\mathrm{i}k_0 - \frac{1}{2r}\right)v + \frac{\partial v}{\partial r}\right) - \frac{\partial_\theta s}{r^2}\frac{\partial v}{\partial \theta}\right](r,\theta,s^+(r,\theta)),$$

or equivalently, for $r \gg 0$,

$$\frac{1}{\rho_{\mathrm{w}}}\left[\frac{\partial v}{\partial z} - \partial_r s\left(\mathrm{i}k_0 v + \frac{\partial v}{\partial r}\right) - \frac{\partial_\theta s}{r^2}\frac{\partial v}{\partial \theta}\right](r,\theta,s^-(r,\theta))$$
$$= \frac{1}{\rho_{\mathrm{s}}}\left[\frac{\partial v}{\partial z} - \partial_r s\left(\mathrm{i}k_0 v + \frac{\partial v}{\partial r}\right) - \frac{\partial_\theta s}{r^2}\frac{\partial v}{\partial \theta}\right](r,\theta,s^+(r,\theta)).$$

Neither of these two interface conditions is compatible with the parabolic equation (6) due to the $\partial/\partial r$-derivative terms. In other words, it means that using the boundary condition derived directly from the normal derivative conditions given by Eq. (3), which is mathematically correct for the 3D Helmholtz equation, would lead with Eq. (6) to an ill-posed initial- and boundary-valued problem due to the fact that the stability condition (17) would not be satisfied.

3. The Transformed 3D Narrow-Angle PE Model

3.1. *The transformed initial and boundary value problem*

In this section the initial and boundary value problem (6)–(11), (15), (16) which holds in a range varying physical domain, is transformed, using an appropriate change-of-variable technique, to a new one on a cylindrical domain. For this purpose, the following azimuth- and range-dependent change of the depth variable (analog to the range-dependent change of variable used in Ref. 34) is introduced:

$$\xi = \begin{cases} \dfrac{s_*}{s(r,\theta)}\,z, & 0 \le z \le s(r,\theta), \\ z_{\mathrm{abs}} - \left(\dfrac{z_{\mathrm{abs}} - s_*}{z_{\mathrm{abs}} - s(r,\theta)}\right)(z_{\mathrm{abs}} - z), & s(r,\theta) \le z \le z_{\mathrm{abs}}, \\ z, & z_{\mathrm{abs}} \le z \le z_{\max}, \end{cases} \tag{18}$$

where $s_* = s(0,0)$, that sends the azimuth- and range-dependent interval $[0, s(r,\theta)]$ (respectively $[s(r,\theta), z_{\mathrm{abs}}]$) onto the interval $[0, s_*]$ (resp. onto $[s_*, z_{\mathrm{abs}}]$). The transformed domain is described by the variables r, θ, and ξ. The first two, r and θ, are kept unchanged: the horizontal range r varies from 0 to $r_{\max}$ and the azimuthal angle θ varies from 0 to 2π. The transformed "depth" ξ varies from 0 to $z_{\max}$. The transformed waveguide is now bounded in "depth" by two flat surfaces at $\{\xi = 0\}$ and $\{\xi = z_{\max}\}$, and two flat sediment interfaces at $\{\xi = s_*\}$ and $\{\xi = z_{\mathrm{abs}}\}$. One important feature of the change of variable used here, is that

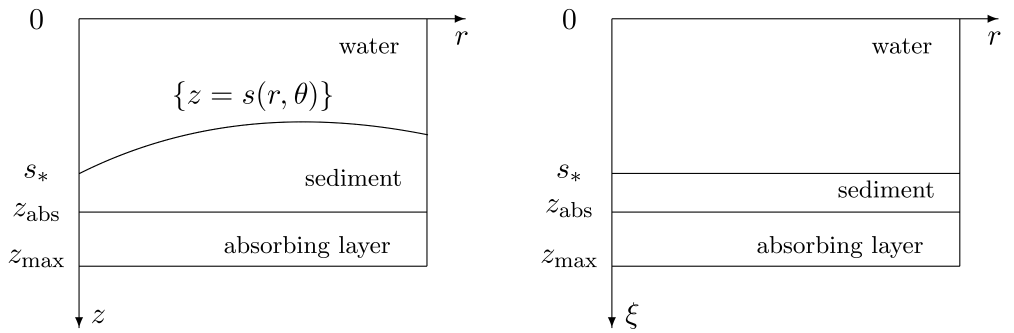

Fig. 1. Schematic (vertical slice at constant azimuth) of the real multilayered domain (left subplot) and of the transformed multilayered domain (right subplot).

it can handle general interfaces. This extends the change of variable used in Ref. 25, where it was required that the interfaces $\Sigma_{\rm sed}$ and $\Sigma_{\rm abs}$ be homothetical in the physical domain. The inverse change of variable is given by:

$$z = \begin{cases} \dfrac{s(r,\theta)}{s_*}\,\xi, & 0 \le \xi \le s_*, \\ z_{\rm abs} - \left(\dfrac{z_{\rm abs} - s(r,\theta)}{z_{\rm abs} - s_*}\right)(z_{\rm abs} - \xi), & s_* \le \xi \le z_{\rm abs}, \\ \xi, & z_{\rm abs} \le \xi \le z_{\rm max}. \end{cases} \tag{19}$$

Let $u = u(r,\theta,\xi)$ denote the new unknown in the transformed domain defined by its restrictions on each of the three layers:

$$u(r,\theta,\xi) = \begin{cases} u_{\rm w}(r,\theta,\xi) = v_{\rm w}\left(r,\theta,\dfrac{s(r,\theta)}{s_*}\,\xi\right), & \xi \in (0, s_*), \\ u_{\rm s}(r,\theta,\xi) = v_{\rm s}\left(r,\theta, z_{\rm abs} - \left(\dfrac{z_{\rm abs} - s(r,\theta)}{z_{\rm abs} - s_*}\right)(z_{\rm abs} - \xi)\right), & \xi \in (s_*, z_{\rm abs}), \\ u_{\rm a}(r,\theta,\xi) = v_{\rm a}(r,\theta,\xi), & \xi \in (z_{\rm abs}, z_{\rm max}). \end{cases}$$

The PDE given in Eq. (6) now becomes (in a compact form):

$$\frac{\partial u}{\partial r} = \frac{\mathrm{i}\rho}{2k_0}\left[\alpha\frac{\partial}{\partial \xi}\left(\frac{1}{\rho}\frac{\partial u}{\partial \xi}\right) + \frac{1}{r^2}\mathcal{L}\left(\frac{1}{\rho}\mathcal{L}u\right)\right] + \mu\partial_r s\,\frac{\partial u}{\partial \xi} + \frac{\mathrm{i}k_0}{2}\tilde{\beta}u, \tag{20}$$

for $r \in [0, r_{\rm max}]$, $\theta \in [0, 2\pi]$, $\xi \in (0, s_*) \cup (s_*, z_{\rm abs}) \cup (z_{\rm abs}, z_{\rm max})$, where

$$\alpha(r,\theta,\xi) = \begin{cases} \alpha_{\rm w}(r,\theta) = (s_*/s(r,\theta))^2, & \xi \in (0, s_*), \\ \alpha_{\rm s}(r,\theta) = ((z_{\rm abs} - s_*)/(z_{\rm abs} - s(r,\theta)))^2, & \xi \in (s_*, z_{\rm abs}), \\ \alpha_{\rm a}(r,\theta) = 1, & \xi \in (z_{\rm abs}, z_{\rm max}), \end{cases}$$

where the operator $\mathcal{L}$ accounts for horizontal refraction and is defined by:

$$\mathcal{L} = \frac{\partial}{\partial \theta} - \mu\partial_\theta s\,\frac{\partial}{\partial \xi},$$

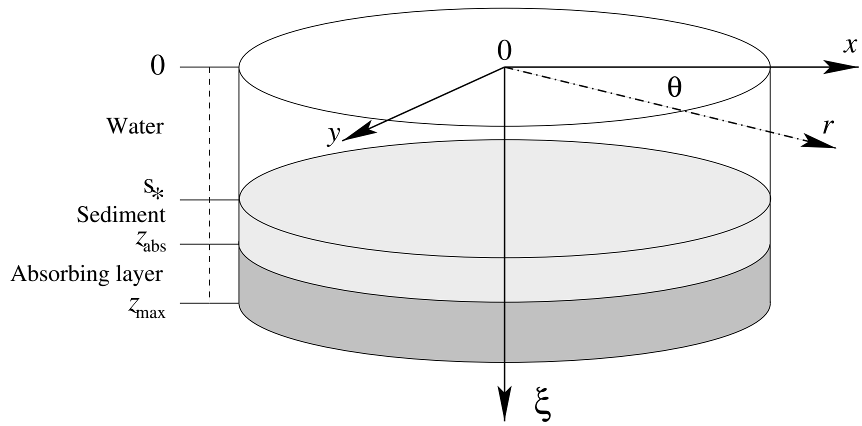

Fig. 2. Cylindrical geometry of the mapped computation domain for $0 \leq r \leq r_{\max}$, $0 \leq \theta \leq 2\pi$, $0 \leq \xi \leq z_{\max}$.

with μ given by:

$$\mu(r,\theta,\xi) = \begin{cases} \mu_{\mathrm{w}}(r,\theta,\xi) = \xi/s(r,\theta), & \xi \in (0, s_*) \\ \mu_{\mathrm{s}}(r,\theta,\xi) = (z_{\mathrm{abs}} - \xi)/(z_{\mathrm{abs}} - s(r,\theta)), & \xi \in (s_*, z_{\mathrm{abs}}), \\ \mu_{\mathrm{a}}(r,\theta,\xi) = 0, & \xi \in (z_{\mathrm{abs}}, z_{\max}), \end{cases}$$

and where

$$\tilde{\beta}(r,\theta,\xi) = \begin{cases} \tilde{\beta}_{\mathrm{w}}(r,\theta,\xi) = \beta_{\mathrm{w}}\left(r,\theta,\dfrac{s(r,\theta)}{s_*}\,\xi\right), & \xi \in (0, s_*), \\ \tilde{\beta}_{\mathrm{s}}(r,\theta,\xi) = \beta_{\mathrm{s}}\left(r,\theta,z_{\mathrm{abs}} - \left(\dfrac{z_{\mathrm{abs}} - s(r,\theta)}{z_{\mathrm{abs}} - s_*}\right)(z_{\mathrm{abs}} - \xi)\right), & \xi \in (s_*, z_{\mathrm{abs}}), \\ \tilde{\beta}_{\mathrm{a}}(r,\theta,\xi) = \beta_{\mathrm{a}}(r,\theta,\xi), & \xi \in (z_{\mathrm{abs}}, z_{\max}). \end{cases}$$

Equation (20) contains new derivative terms and variable coefficients which account for the variations of the bottom topography. The transformed field u satisfies the initial condition:

$$u(0,\theta,\xi) = v^0(\theta,\xi), \qquad \theta \in [0,2\pi], \quad \xi \in [0, z_{\max}], \tag{21}$$

the two pressure-release boundary conditions at $\{\xi = 0\}$ and $\{\xi = z_{\max}\}$:

$$u(r,\theta,0) = u(r,\theta,z_{\max}) = 0, \qquad r \in [0, r_{\max}], \quad \theta \in [0,2\pi], \tag{22}$$

a 2π-periodic condition in azimuth:

$$u(r,0,\xi) = u(r,2\pi,\xi), \qquad r \in [0, r_{\max}], \quad \xi \in [0, z_{\max}], \tag{23}$$

and the following transmission conditions at $\{\xi = s_*\}$:

$$u(r,\theta,s_*^-) = u(r,\theta,s_*^+), \qquad r \in [0, r_{\max}], \quad \theta \in [0,2\pi], \tag{24}$$

$$\frac{1}{\rho_{\mathrm{w}}}\frac{\partial u}{\partial \tilde{T}}(r,\theta,s_*^-) = \frac{1}{\rho_{\mathrm{s}}}\frac{\partial u}{\partial \tilde{T}}(r,\theta,s_*^+), \qquad r \in [0, r_{\max}], \quad \theta \in [0,2\pi], \tag{25}$$

where, for all $(r,\theta) \in [0, r_{\max}] \times [0, 2\pi]$,

$$\frac{\partial}{\partial \tilde{T}} = \begin{cases} \dfrac{s_*}{s}\dfrac{\partial}{\partial \xi} - \mathrm{i}k_0 \partial_r s \mathcal{I} - \dfrac{\partial_\theta s}{r^2}\left(\dfrac{\partial}{\partial \theta} - \mu_{\mathrm{w}} \partial_\theta s \dfrac{\partial}{\partial \xi}\right), & \xi = s_*^-, \\ \left(\dfrac{z_{\mathrm{abs}} - s_*}{z_{\mathrm{abs}} - s}\right)\dfrac{\partial}{\partial \xi} - \mathrm{i}k_0 \partial_r s \mathcal{I} - \dfrac{\partial_\theta s}{r^2}\left(\dfrac{\partial}{\partial \theta} - \mu_{\mathrm{s}} \partial_\theta s \dfrac{\partial}{\partial \xi}\right), & \xi = s_*^+. \end{cases} \tag{26}$$

Along the artificial interface at $\{\xi = z_{\mathrm{abs}}\}$ the transformed field u satisfies the two transmission conditions:

$$u(r,\theta,z_{\mathrm{abs}}^-) = u(r,\theta,z_{\mathrm{abs}}^+), \qquad r \in [0, r_{\max}], \quad \theta \in [0, 2\pi], \tag{27}$$

$$\frac{1}{\rho_{\mathrm{s}}}\left(\frac{z_{\mathrm{abs}} - s_*}{z_{\mathrm{abs}} - s}\right)\frac{\partial u}{\partial \xi}(r,\theta,z_{\mathrm{abs}}^-) = \frac{1}{\rho_{\mathrm{a}}}\frac{\partial u}{\partial \xi}(r,\theta,z_{\mathrm{abs}}^+), \qquad r \in [0, r_{\max}], \quad \theta \in [0, 2\pi]. \tag{28}$$

3.2. *An energy-conserving weak formulation*

Let $\Omega_{\mathrm{w}} := (0, s_*) \times (0, 2\pi)$, $\Omega_{\mathrm{s}} := (s_*, z_{\mathrm{abs}}) \times (0, 2\pi)$, $\Omega_{\mathrm{a}} := (z_{\mathrm{abs}}, z_{\max}) \times (0, 2\pi)$, and $\Omega = \Omega_{\mathrm{w}} \cup \Omega_{\mathrm{s}} \cup \Omega_{\mathrm{a}}$. Let $\Gamma_* := \{s_*\} \times (0, 2\pi)$, $\Gamma_{\mathrm{abs}} := \{z_{\mathrm{abs}}\} \times (0, 2\pi)$. We introduce a new term $\varepsilon = \varepsilon(r,\theta,\xi)$ defined by:

$$\varepsilon(r,\theta,\xi) = \begin{cases} \varepsilon_{\mathrm{w}}(r,\theta) = s(r,\theta)/s_*, & \xi \in (0, s_*), \\ \varepsilon_{\mathrm{s}}(r,\theta) = (z_{\mathrm{abs}} - s(r,\theta))/(z_{\mathrm{abs}} - s_*), & \xi \in (s_*, z_{\mathrm{abs}}), \\ \varepsilon_{\mathrm{a}}(r,\theta) = 1, & \xi \in (z_{\mathrm{abs}}, z_{\max}), \end{cases} \tag{29}$$

and for the sake of brevity, we use the following compact notation:

$$\int_\Omega \phi\,\bar{\varphi}\,\frac{\varepsilon\,\mathrm{d}\Omega}{\rho} := \int_{\Omega_{\mathrm{w}}} \phi_{\mathrm{w}}\,\bar{\varphi}_{\mathrm{w}}\,\frac{\varepsilon_{\mathrm{w}}\,\mathrm{d}\Omega}{\rho_{\mathrm{w}}} + \int_{\Omega_{\mathrm{s}}} \phi_{\mathrm{s}}\,\bar{\varphi}_{\mathrm{s}}\,\frac{\varepsilon_{\mathrm{s}}\,\mathrm{d}\Omega}{\rho_{\mathrm{s}}} + \int_{\Omega_{\mathrm{a}}} \phi_{\mathrm{a}}\,\bar{\varphi}_{\mathrm{a}}\,\frac{\varepsilon_{\mathrm{a}}\,\mathrm{d}\Omega}{\rho_{\mathrm{a}}}$$

for $\phi, \varphi \in L^2(\Omega)$, $r \in (0, r_{\max})$, where an overbar denotes complex conjugation, and where $\rho = \rho_{\mathrm{w}}$ if $\xi \in (0, s_*)$, $\rho = \rho_{\mathrm{s}}$ if $\xi \in (s_*, z_{\mathrm{abs}})$, and $\rho = \rho_{\mathrm{a}}$ if $\xi \in (z_{\mathrm{abs}}, z_{\max})$. Let u be the solution of (20)–(28) and ψ denote an arbitrary smooth function on $\bar{\Omega}$ which satisfies a zero Dirichlet condition at $\xi = 0$ and $\xi = z_{\max}$, and a 2π-periodicity in azimuth. Multiplying both sides of Eq. (20) by $\bar{\psi}\varepsilon/\rho$, we obtain:

$$\begin{aligned} \int_\Omega \frac{\partial u}{\partial r}\bar{\psi}\,\frac{\varepsilon\,\mathrm{d}\Omega}{\rho} &= \frac{\mathrm{i}}{2k_0}\int_\Omega \left(\alpha\frac{\partial}{\partial \xi}\left(\frac{1}{\rho}\frac{\partial u}{\partial \xi}\right)\bar{\psi} + \frac{1}{r^2}\mathcal{L}\left(\frac{1}{\rho}\mathcal{L}u\right)\bar{\psi}\right)\varepsilon\,\mathrm{d}\Omega \\ &\quad + \int_\Omega \mu \partial_r s\,\frac{\partial u}{\partial \xi}\,\bar{\psi}\,\frac{\varepsilon\,\mathrm{d}\Omega}{\rho} + \frac{\mathrm{i}k_0}{2}\int_\Omega \tilde{\beta} u \bar{\psi}\,\frac{\varepsilon\,\mathrm{d}\Omega}{\rho}. \end{aligned} \tag{30}$$

Let us focus on the first integral term on the right hand side of Eq. (30). Integrating by parts, we obtain:

$$\int_\Omega \alpha \frac{\partial}{\partial \xi}\left(\frac{1}{\rho}\frac{\partial u}{\partial \xi}\right)\bar{\psi}\varepsilon \mathrm{d}\Omega = -\int_\Omega \alpha \frac{\partial u}{\partial \xi}\frac{\partial \bar{\psi}}{\partial \xi}\frac{\varepsilon\,\mathrm{d}\Omega}{\rho} + \int_{\Gamma_*}\left(\frac{1}{\rho_\mathrm{w}}\left(\frac{s_*}{s}\right)\frac{\partial u_\mathrm{w}}{\partial \xi} - \frac{1}{\rho_\mathrm{s}}\left(\frac{z_\mathrm{abs}-s_*}{z_\mathrm{abs}-s}\right)\frac{\partial u_\mathrm{s}}{\partial \xi}\right)\bar{\psi}\,\mathrm{d}\Gamma + \int_{\Gamma_\mathrm{abs}}\left(\frac{1}{\rho_\mathrm{s}}\left(\frac{z_\mathrm{abs}-s_*}{z_\mathrm{abs}-s}\right)\frac{\partial u_\mathrm{s}}{\partial \xi} - \frac{1}{\rho_\mathrm{a}}\frac{\partial u_\mathrm{a}}{\partial \xi}\right)\bar{\psi}\,\mathrm{d}\Gamma. \tag{31}$$

In the same way, integrating by parts and using the 2π-periodicity of s and u, we get:

$$\int_\Omega \mathcal{L}\left(\frac{1}{\rho}\mathcal{L}u\right)\bar{\psi}\varepsilon\mathrm{d}\Omega = -\int_\Omega (\mathcal{L}u)(\mathcal{L}\bar{\psi})\frac{\varepsilon\,\mathrm{d}\Omega}{\rho} + \int_{\Gamma_*}\left(-\frac{\partial_\theta s}{\rho_\mathrm{w}}\left(\frac{\partial u_\mathrm{w}}{\partial \theta} - \mu_\mathrm{w}\partial_\theta s\frac{\partial u_\mathrm{w}}{\partial \xi}\right) + \frac{\partial_\theta s}{\rho_\mathrm{s}}\left(\frac{\partial u_\mathrm{s}}{\partial \theta} - \mu_\mathrm{s}\partial_\theta s\frac{\partial u_\mathrm{s}}{\partial \xi}\right)\right)\bar{\psi}\,\mathrm{d}\Gamma. \tag{32}$$

Multiplying (32) by r^{-2}, summing with (31) and using transmission conditions (25) and (28) at $\{\xi = s_*\}$ and $\{\xi = z_\mathrm{abs}\}$ respectively, we derive:

$$\int_\Omega \left(\alpha\frac{\partial}{\partial \xi}\left(\frac{1}{\rho}\frac{\partial u}{\partial \xi}\right) + \frac{1}{r^2}\mathcal{L}\left(\frac{1}{\rho}\mathcal{L}u\right)\right)\bar{\psi}\varepsilon\mathrm{d}\Omega = -\int_\Omega\left(\alpha\frac{\partial u}{\partial \xi}\frac{\partial \bar{\psi}}{\partial \xi} + \frac{1}{r^2}(\mathcal{L}u)(\mathcal{L}\bar{\psi})\right)\frac{\varepsilon\,\mathrm{d}\Omega}{\rho} + \int_{\Gamma_*}\mathrm{i}k_0\partial_r s\left(\frac{u_\mathrm{w}}{\rho_\mathrm{w}} - \frac{u_\mathrm{s}}{\rho_\mathrm{s}}\right)\bar{\psi}\,\mathrm{d}\Gamma. \tag{33}$$

Using (33) in (30), we obtain:

$$\int_\Omega \frac{\partial u}{\partial r}\bar{\psi}\frac{\varepsilon\,\mathrm{d}\Omega}{\rho} = -\frac{\mathrm{i}}{2k_0}\int_\Omega\left(\alpha\frac{\partial u}{\partial \xi}\frac{\partial \bar{\psi}}{\partial \xi} + \frac{1}{r^2}(\mathcal{L}u)(\mathcal{L}\bar{\psi})\right)\frac{\varepsilon\,\mathrm{d}\Omega}{\rho} + \int_\Omega \mu\,\partial_r s\,\frac{\partial u}{\partial \xi}\,\bar{\psi}\,\frac{\varepsilon\,\mathrm{d}\Omega}{\rho} + \frac{\mathrm{i}k_0}{2}\int_\Omega \tilde{\beta}u\bar{\psi}\,\frac{\varepsilon\,\mathrm{d}\Omega}{\rho} - \frac{1}{2}\int_{\Gamma_*}\partial_r s\left(\frac{u_\mathrm{w}}{\rho_\mathrm{w}} - \frac{u_\mathrm{s}}{\rho_\mathrm{s}}\right)\bar{\psi}\,\mathrm{d}\Gamma. \tag{34}$$

Using integration by parts, one can easily check that:

$$\int_\Omega \mu\,\partial_r s\,\frac{\partial u}{\partial \xi}\,\bar{\psi}\,\frac{\varepsilon\mathrm{d}\Omega}{\rho} = \frac{1}{2}\int_\Omega \mu\,\partial_r s\left(\frac{\partial u}{\partial \xi}\,\bar{\psi} - u\,\frac{\partial \bar{\psi}}{\partial \xi}\right)\frac{\varepsilon\,\mathrm{d}\Omega}{\rho} - \frac{1}{2}\int_\Omega (\partial_\xi \mu)(\partial_r s)u\bar{\psi}\,\frac{\varepsilon\,\mathrm{d}\Omega}{\rho} + \frac{1}{2}\int_{\Gamma_*}\partial_r s\left(\frac{u_\mathrm{w}}{\rho_\mathrm{w}} - \frac{u_\mathrm{s}}{\rho_\mathrm{s}}\right)\bar{\psi}\,\mathrm{d}\Gamma. \tag{35}$$

Now, using (35) in (34), the integral on Γ_* vanishes and we have:

$$\begin{aligned}\int_\Omega \left(\frac{\partial u}{\partial r} + \frac{1}{2}(\partial_\xi \mu)(\partial_r s)u\right)\bar{\psi}\,\frac{\varepsilon\,\mathrm{d}\Omega}{\rho} &= -\frac{\mathrm{i}}{2k_0}\int_\Omega \left(\alpha \frac{\partial u}{\partial \xi}\frac{\partial \bar{\psi}}{\partial \xi} + \frac{1}{r^2}(\mathcal{L}u)(\mathcal{L}\bar{\psi})\right)\frac{\varepsilon\,\mathrm{d}\Omega}{\rho}\\ &\quad + \frac{1}{2}\int_\Omega \mu\partial_r s\left(\frac{\partial u}{\partial \xi}\bar{\psi} - u\frac{\partial \bar{\psi}}{\partial \xi}\right)\frac{\varepsilon\,\mathrm{d}\Omega}{\rho}\\ &\quad + \frac{\mathrm{i}k_0}{2}\int_\Omega \tilde{\beta} u\bar{\psi}\,\frac{\varepsilon\,\mathrm{d}\Omega}{\rho}. \end{aligned} \tag{36}$$

Let us denote by $\langle\cdot,\cdot\rangle_{\rho,\varepsilon}$ the (natural to the problem at hand) weighted r-dependent L^2-inner product defined for $\phi, \varphi \in L^2(\Omega)$, $r \in (0, r_{\max})$, by:

$$\langle \phi, \varphi\rangle_{\rho,\varepsilon} = \int_\Omega \phi\bar{\varphi}\,\frac{\varepsilon\,\mathrm{d}\Omega}{\rho}. \tag{37}$$

In what follows, $\|\cdot\|_{\rho,\varepsilon}$ will denote the weighted norm on $L^2(\Omega)$ induced by the inner product $\langle\cdot,\cdot\rangle_{\rho,\varepsilon}$. We have thus obtained a weak form of our problem which consists in finding $u(r) \in V$ satisfying for $r \in (0, r_{\max})$,

$$\left\langle \frac{\partial u}{\partial r} + \frac{1}{2}(\partial_\xi\mu)(\partial_r s)u, \psi\right\rangle_{\rho,\varepsilon} + \mathrm{i}a(r; u, \psi) + \frac{k_0}{2}\langle \mathrm{Im}(\tilde{\beta}(r))u, \psi\rangle_{\rho,\varepsilon} = 0, \quad \forall \psi \in V, \tag{38}$$

and $u(0) = u^0$, $(\theta, \xi) \in (0, 2\pi) \times (0, z_{\max})$. In (38), V denotes the linear space of functions which belong to $H^1(\Omega)$ and which satisfy a zero Dirichlet condition on $\xi = 0$ and $\xi = z_{\max}$, and a 2π-periodicity in azimuth. Here, we suppress both $\theta-$ and $\xi-$ dependencies in the argument of various functions, writing, for example, $u(r) = u(r,\cdot,\cdot)$, $\tilde{\beta}(r) = \tilde{\beta}(r,\cdot,\cdot)$, etc. The r-dependent sesquilinear form $a(r;\cdot,\cdot) : V \times V \to \mathrm{C}$ in (38) is defined by

$$\begin{aligned} a(r;\phi,\varphi) &= \frac{1}{2k_0}\left(\left\langle \alpha\frac{\partial\phi}{\partial\xi}, \frac{\partial\varphi}{\partial\xi}\right\rangle_{\rho,\varepsilon} + \frac{1}{r^2}\langle \mathcal{L}\phi, \mathcal{L}\varphi\rangle_{\rho,\varepsilon}\right)\\ &\quad + \frac{\mathrm{i}}{2}\left[\left\langle \mu\partial_r s\frac{\partial\phi}{\partial\xi}, \varphi\right\rangle_{\rho,\varepsilon} - \left\langle \mu\partial_r s\phi, \frac{\partial\varphi}{\partial\xi}\right\rangle_{\rho,\varepsilon}\right] - \frac{k_0}{2}\langle \mathrm{Re}(\tilde{\beta}(r))\phi, \varphi\rangle_{\rho,\varepsilon}, \end{aligned} \tag{39}$$

for $\phi, \varphi \in V$, $r \in (0, r_{\max})$. It is now straightforward to show that the transformed field u satisfies the energy-conservation formula (17). Indeed, starting from

$$\frac{\partial u}{\partial r} + \frac{1}{2}(\partial_\xi\mu)(\partial_r s)u = \frac{1}{\sqrt{\varepsilon}}\frac{\partial(\sqrt{\varepsilon}u)}{\partial r},$$

taking $\psi = u(r)$ in the variational equality given in (38), using the fact that:

$$\left\langle \frac{1}{\sqrt{\varepsilon}}\frac{\partial(\sqrt{\varepsilon}u)}{\partial r}, u\right\rangle_{\rho,\varepsilon} = \frac{1}{2}\frac{\mathrm{d}}{\mathrm{d}r}\|u\|^2_{\rho,\varepsilon} + \mathrm{i} \times \mathrm{Im}\left(\left\langle \frac{1}{\sqrt{\varepsilon}}\frac{\partial(\sqrt{\varepsilon}u)}{\partial r}, u\right\rangle_{\rho,\varepsilon}\right),$$

and taking real parts, we obtain that:

$$\frac{1}{2}\frac{\mathrm{d}}{\mathrm{d}r}\|u(r)\|^2_{\rho,\varepsilon} = -\frac{k_0}{2}\langle \mathrm{Im}(\tilde{\beta}(r))u(r), u(r)\rangle_{\rho,\varepsilon}.$$

Since $\mathrm{Im}(\tilde{\beta}(r)) \geq 0$, this yields:

$$\frac{\mathrm{d}}{\mathrm{d}r}\|u(r)\|_{\rho,\varepsilon} \leq 0, \quad 0 \leq r \leq r_{\max}. \tag{40}$$

Therefore, if $\mathrm{Im}(\tilde{\beta}(r)) \not\equiv 0$, the following dissipation property holds for the solution of (20)–(28):

$$\|u(r_2)\|_{\rho,\varepsilon} \leq \|u(r_1)\|_{\rho,\varepsilon}, \quad 0 \leq r_1 \leq r_2 \leq r_{\max}.$$

If $\mathrm{Im}(\tilde{\beta}(r)) \equiv 0$, the above dissipation property is replaced by the conservation of the $\|\cdot\|_{\rho,\varepsilon}$ norm.

4. Numerical Scheme

In this section we shall discretize the transformed initial and boundary value problem (20)–(28) using the standard Galerkin/Finite-Element method with piecewise linear continuous functions in ξ and θ, coupled with the conservative Crank–Nicolson marching scheme to discretize in range.

4.1. *The fully discrete scheme*

Let $\{\theta_0, \theta_1, \ldots, \theta_M\}$ be a uniform partition of $[0, 2\pi]$, where $\theta_m = m\Delta\theta$, $0 \leq m \leq M$, with $\Delta\theta = 2\pi/M$, $\theta_0 = 0$, and $\theta_M = 2\pi$. Let also $\{\xi_0, \xi_1, \ldots, \xi_{N+1}\}$ be a partition of $[0, z_{\max}]$, such that $\xi_{n'} = s_*$ and $\xi_{n''} = z_{\mathrm{abs}}$ for some integers n' and n'' satisfying $1 < n' < n'' < N+1$, $\xi_0 = 0$ and $\xi_{N+1} = z_{\max}$. Moreover, we assume a partitioning of $[0, s_*]$, $[s_*, z_{\mathrm{abs}}]$ and $[z_{\mathrm{abs}}, z_{\max}]$, with uniform mesh lengths $\Delta\xi_{\mathrm{w}}$, $\Delta\xi_{\mathrm{s}}$ and $\Delta\xi_{\mathrm{a}}$ respectively. We denote by $P_{m,n} = (\theta_m, \xi_n)$ a node of the grid. For $0 \leq m \leq M$, the nodes $P_{m,0}$ and $P_{m,N+1}$, lie on $\{\xi = 0\}$ and $\{\xi = z_{\max}\}$ respectively. The nodes $P_{m,n'}$ and $P_{m,n''}$, for $0 \leq m \leq M$, lie on $\{\xi = s_*\}$ and $\{\xi = z_{\mathrm{abs}}\}$, respectively. For $1 \leq m \leq M$, $1 \leq n \leq N+1$, we let:

$$\mathcal{K}_{m,n} =]\theta_{m-1}, \theta_m[\times]\xi_{n-1}, \xi_n[$$

so that $\bar{\Omega} = \cup_{1\leq m\leq M,\, 1\leq n\leq N+1} \bar{\mathcal{K}}_{m,n}$ and $\mathcal{K}_{m,n} \cap \mathcal{K}_{\tilde{m},\tilde{n}} = \emptyset$ if $(m,n) \neq (\tilde{m},\tilde{n})$. Let Q_1 be the space of complex-valued polynomials of degree at most 1 in ξ and θ. We define the finite dimensional vector space V_h of complex-valued functions which are continuous on $\bar{\Omega}$, piecewise Q_1-polynomial relatively to each mesh $\mathcal{K}_{m,n}$, $1 \leq m \leq M$, $1 \leq n \leq N+1$, satisfy the homogeneous Dirichlet conditions at both $\xi = 0$ and $\xi = z_{\max}$, and are 2π-periodic in azimuth, i.e.:

$$\begin{aligned} V_h = \{\psi \mid \psi \in C^0(\bar{\Omega}) \text{ complex-valued, } \psi|_{\mathcal{K}_{m,n}} \in Q_1 \text{ for } 1 \leq m \leq M,\ 1 \leq n \leq N+1, \\ \psi \text{ is } 2\pi\text{-periodic, } \psi|_{\xi=0} = \psi|_{\xi=z_{\max}} = 0\}. \end{aligned}$$

The vector space V_h is a subspace of V such that $\dim V_h = MN$. Let $K = MN$. For $\Delta r > 0$ so that $r_{\max} = L\Delta r$, we let $r^\ell = \ell\Delta r$, $0 \leq \ell \leq L$, and $r^{\ell+\frac{1}{2}} = r^\ell + \Delta r/2$, $0 \leq n \leq L-1$.

We consider the following finite element (in depth and azimuth) and Crank–Nicolson (in range) discrete scheme: Find $U^\ell \in V_h$, $1 \le \ell \le L$, such that for $0 \le \ell \le L-1$,

$$\left\langle \frac{U^{\ell+1}-U^\ell}{\Delta r} + \frac{1}{2}((\partial_\xi \mu)(\partial_r s))^{\ell+\frac{1}{2}} \frac{U^{\ell+1}+U^\ell}{2}, \psi_h \right\rangle_{\rho,\varepsilon^{\ell+\frac{1}{2}}}$$
$$+ \mathrm{i}a\left(r^{\ell+\frac{1}{2}}; \frac{U^{\ell+1}+U^\ell}{2}, \psi_h\right) + \frac{k_0}{2}\left\langle \mathrm{Im}(\tilde{\beta}^{\ell+\frac{1}{2}})\frac{U^{\ell+1}+U^\ell}{2}, \psi_h \right\rangle_{\rho,\varepsilon^{\ell+\frac{1}{2}}} = 0, \quad (41)$$

for all $\psi_h \in V_h$, and $U^0 = u^0$. For $1 \le k \le K$, we let $P_k = P_{m,n}$ with $k = m + M(n-1)$, $1 \le m \le M$, $1 \le n \le N$. This corresponds to numbering the grid nodes along θ at constant ξ. Let $\{\psi_k\}$, $1 \le k \le K$ be the finite element basis defined by $\psi_k(P_{k'}) = 0$ if $k \ne k'$ and $\psi_k(P_k) = 1$. Then,

$$U^\ell = \sum_{k=1}^{K} U_k^\ell \psi_k, \quad 0 \le \ell \le L,$$

and, for $0 \le \ell \le L$, $U^\ell(P_k) = U_k^\ell$, $1 \le k \le K$. For $0 \le \ell \le L$, we construct the vector $\mathbf{U}^\ell$ of dimension K, whose kth component is the value of function U^ℓ at grid point $P_{m,n}$ such that $k = m + M(n-1)$. By letting $U_{m,n}^\ell = U^\ell(P_{m,n})$ for $1 \le m \le M$, $1 \le n \le N$, the vector $\mathbf{U}^\ell$ is defined by:

$$\mathbf{U}^\ell = (\underbrace{U_{1,1}^\ell, U_{2,1}^\ell, \ldots, U_{M,1}^\ell}_{n=1}, \underbrace{U_{1,2}^\ell, U_{2,2}^\ell, \ldots, U_{M,2}^\ell}_{n=2}, \ldots, \underbrace{U_{1,N}^\ell, U_{2,N}^\ell, \ldots, U_{M,N}^\ell}_{n=N})^T.$$

It is then straightforward to show that (41) can be written in a matrix-vector form as follows

$$\left(\mathrm{G}^{\ell+\frac{1}{2}} + \mathrm{i}\frac{\Delta r}{2}(\mathrm{T}^{\ell+\frac{1}{2}} + \mathrm{S}^{\ell+\frac{1}{2}})\right)\mathbf{U}^{\ell+1} = \left(\mathrm{G}^{\ell+\frac{1}{2}} - \mathrm{i}\frac{\Delta r}{2}(\mathrm{T}^{\ell+\frac{1}{2}} + \mathrm{S}^{\ell+\frac{1}{2}})\right)\mathbf{U}^{\ell}, \quad (42)$$

for $0 \le \ell \le L-1$, where $\mathrm{G}^{\ell+\frac{1}{2}}$ is the mass matrix of the finite element basis at range $r^{\ell+\frac{1}{2}}$,

$$\mathrm{G}_{k,k'}^{\ell+\frac{1}{2}} = \int_\Omega \psi_{k'}\bar{\psi}_k \frac{\varepsilon^{\ell+\frac{1}{2}}\mathrm{d}\Omega}{\rho}, \qquad 1 \le k, \quad k' \le K,$$

and where $\mathrm{T}^{\ell+\frac{1}{2}}$ and $\mathrm{S}^{\ell+\frac{1}{2}}$, $0 \le \ell \le L-1$, are Kth order square matrices with components defined by:

$$\mathrm{T}_{k,k'}^{\ell+\frac{1}{2}} = \frac{1}{2k_0}\int_\Omega \alpha^{\ell+\frac{1}{2}}\frac{\partial\psi_{k'}}{\partial\xi}\frac{\partial\bar{\psi}_k}{\partial\xi}\frac{\varepsilon^{\ell+\frac{1}{2}}\mathrm{d}\Omega}{\rho} + \frac{\mathrm{i}}{2}\int_\Omega (\mu\partial_r s)^{\ell+\frac{1}{2}}\left(\frac{\partial\psi_{k'}}{\partial\xi}\bar{\psi}_k - \psi_{k'}\frac{\partial\bar{\psi}_k}{\partial\xi}\right)\frac{\varepsilon^{\ell+\frac{1}{2}}\mathrm{d}\Omega}{\rho}$$
$$- \int_\Omega \left(\frac{k_0}{2}\tilde{\beta}^{\ell+\frac{1}{2}} + \frac{\mathrm{i}}{2}((\partial_\xi\mu)(\partial_r s))^{\ell+\frac{1}{2}}\right)\psi_{k'}\bar{\psi}_k\frac{\varepsilon^{\ell+\frac{1}{2}}\mathrm{d}\Omega}{\rho}, \qquad 1 \le k, \quad k' \le K,$$

$$\mathrm{S}_{k,k'}^{\ell+\frac{1}{2}} = \frac{1}{2k_0(r^{\ell+\frac{1}{2}})^2}\int_\Omega (\mathcal{L}^{\ell+\frac{1}{2}}\psi_{k'})(\mathcal{L}^{\ell+\frac{1}{2}}\bar{\psi}_k)\frac{\varepsilon^{\ell+\frac{1}{2}}\mathrm{d}\Omega}{\rho}, \qquad 1 \le k, \quad k' \le K.$$

Instead of computing exactly the integrals defining the components of $\mathrm{G}^{\ell+\frac{1}{2}}$, $\mathrm{T}^{\ell+\frac{1}{2}}$, and $\mathrm{S}^{\ell+\frac{1}{2}}$, $0 \leq \ell \leq L-1$, we evaluate them approximately using in each mesh $\mathcal{K}_{m,n}$ the following trapezoidal quadrature rule:

$$\int_{\mathcal{K}_{m,n}} \psi \,\mathrm{d}\Omega \approx \frac{\Delta\theta\Delta\xi}{4}(\psi(P_{m-1,n-1}) + \psi(P_{m-1,n}) + \psi(P_{m,n-1}) + \psi(P_{m,n})).$$

Therefore, (42) now becomes:

$$\left(\mathrm{I} + \mathrm{i}\frac{\Delta r}{2}(\tilde{\mathrm{T}}^{\ell+\frac{1}{2}} + \tilde{\mathrm{S}}^{\ell+\frac{1}{2}})\right)\mathbf{U}^{\ell+1} = \left(\mathrm{I} - \mathrm{i}\frac{\Delta r}{2}(\tilde{\mathrm{T}}^{\ell+\frac{1}{2}} + \tilde{\mathrm{S}}^{\ell+\frac{1}{2}})\right)\mathbf{U}^{\ell}, \tag{43}$$

for $0 \leq \ell \leq L-1$, where I is the Kth order identity matrix, $\tilde{\mathrm{T}}^{\ell+\frac{1}{2}}$, $0 \leq \ell \leq L-1$, are 3-diagonal matrices of order K, and $\tilde{\mathrm{S}}^{\ell+\frac{1}{2}}$, $0 \leq \ell \leq L-1$, are 9-diagonal matrices of order K. For $\ell \in \{0, \ldots, L-1\}$, matrices $\tilde{\mathrm{T}}^{\ell+\frac{1}{2}}$ and $\tilde{\mathrm{S}}^{\ell+\frac{1}{2}}$ both possess a block-tridiagonal structure given by:

$$\tilde{\mathrm{T}}^{\ell+\frac{1}{2}} = \begin{pmatrix} \tilde{\mathrm{T}}^{\ell+\frac{1}{2}}_{(1,1)} & \tilde{\mathrm{T}}^{\ell+\frac{1}{2}}_{(1,2)} & & & \\ \tilde{\mathrm{T}}^{\ell+\frac{1}{2}}_{(2,1)} & \tilde{\mathrm{T}}^{\ell+\frac{1}{2}}_{(2,2)} & \tilde{\mathrm{T}}^{\ell+\frac{1}{2}}_{(2,3)} & & \\ & \ddots & \ddots & \ddots & \\ & & \tilde{\mathrm{T}}^{\ell+\frac{1}{2}}_{(N-1,N-2)} & \tilde{\mathrm{T}}^{\ell+\frac{1}{2}}_{(N-1,N-1)} & \tilde{\mathrm{T}}^{\ell+\frac{1}{2}}_{(N-1,N)} \\ & & & \tilde{\mathrm{T}}^{\ell+\frac{1}{2}}_{(N,N-1)} & \tilde{\mathrm{T}}^{\ell+\frac{1}{2}}_{(N,N)} \end{pmatrix}, \tag{44}$$

$$\tilde{\mathrm{S}}^{\ell+\frac{1}{2}} = \frac{1}{2k_0(r^{\ell+\frac{1}{2}})^2}\begin{pmatrix} \tilde{\mathrm{S}}^{\ell+\frac{1}{2}}_{(1,1)} & \tilde{\mathrm{S}}^{\ell+\frac{1}{2}}_{(1,2)} & & & \\ \tilde{\mathrm{S}}^{\ell+\frac{1}{2}}_{(2,1)} & \tilde{\mathrm{S}}^{\ell+\frac{1}{2}}_{(2,2)} & \tilde{\mathrm{S}}^{\ell+\frac{1}{2}}_{(2,3)} & & \\ & \ddots & \ddots & \ddots & \\ & & \tilde{\mathrm{S}}^{\ell+\frac{1}{2}}_{(N-1,N-2)} & \tilde{\mathrm{S}}^{\ell+\frac{1}{2}}_{(N-1,N-1)} & \tilde{\mathrm{S}}^{\ell+\frac{1}{2}}_{(N-1,N)} \\ & & & \tilde{\mathrm{S}}^{\ell+\frac{1}{2}}_{(N,N-1)} & \tilde{\mathrm{S}}^{\ell+\frac{1}{2}}_{(N,N)} \end{pmatrix}. \tag{45}$$

All the blocks of $\tilde{\mathrm{T}}^{\ell+\frac{1}{2}}$ are diagonal matrices of order M, while all the blocks of $\tilde{\mathrm{S}}^{\ell+\frac{1}{2}}$ are tridiagonal matrices of order M, with entries in the upper right and lower left corners (due to the periodicity condition in azimuth). Components of these matrices are given in Appendix. Both $\tilde{\mathrm{T}}^{\ell+\frac{1}{2}}$ and $\tilde{\mathrm{S}}^{\ell+\frac{1}{2}}$ are sparse matrices. Storing $\tilde{\mathrm{T}}^{\ell+\frac{1}{2}}$ (resp. $\tilde{\mathrm{S}}^{\ell+\frac{1}{2}}$) requires declaring only 3 (resp. 9) distinct arrays, each of dimension MN. On the other hand, the bandwith of each of these matrices is function of M. Consequently, the use of any direct algorithm (like the Gaussian elimination method) would require an excessive amount of memory storage since storage must be allocated for the bandwidth in each row of the matrix, which would limit significantly the number of mesh points (in depth and azimuth) that can be used. Note that instead of numbering the grid nodes along θ at constant ξ, we could have numbered the grid nodes along ξ at constant θ, resulting in matrices $\tilde{\mathrm{T}}^{\ell+\frac{1}{2}}$, $0 \leq \ell \leq L-1$, with a bandwith equal to 3, but also unfortunately in matrices $\tilde{\mathrm{S}}^{\ell+\frac{1}{2}}$, $0 \leq \ell \leq L-1$, with a bandwith function of N. Again, the use of any direct algorithm would not be possible due to memory storage limitation. Instead, the inversion of the linear system present in Eq. (43) is performed using an iterative (indirect) algorithm at each step in range. This algorithm is presented in detail in the following section.

4.2. *Use of a non-stationary iterative solver*

As seen in the previous section, the discretization of the continuous problem leads to solving, at each step in range, a system of equations of the form:

$$\mathrm{A}\hat{\mathbf{x}} = \mathbf{b} \tag{46}$$

where A is a nonsingular, large, 9-diagonal matrix of order $K = MN$ with complex elements,

$$\mathrm{A} = \mathrm{I} + \mathrm{i}\frac{\Delta r}{2}(\tilde{\mathrm{T}}^{\ell+\frac{1}{2}} + \tilde{\mathrm{S}}^{\ell+\frac{1}{2}}),$$

and where $\hat{\mathbf{x}}$ and $\mathbf{b}$ are vectors of $\mathbb{C}^K$. In order to effectively utilize the sparseness of matrix A present in the left hand side of (46), it is important to use an iterative (indirect) algorithm. However, since A is neither hermitian, nor definite positive, it is difficult to invert A by use of standard iterative methods (like for instance the conjugate gradient method). Thus, instead of (46), one can consider:

$$\mathrm{A}^*\mathrm{A}\hat{\mathbf{x}} = \mathrm{A}^*\mathbf{b}, \tag{47}$$

where A^* denotes the adjoint of A (i.e. complex conjugation and transposition of matrix A). This equation is known as the *normal equation* and can be derived by simply multiplying (46) by A^*. Equivalently, by letting $\hat{\mathbf{x}} = \mathrm{A}^*\hat{\mathbf{y}}$ in (46), one can consider:

$$\mathrm{A}\mathrm{A}^*\hat{\mathbf{y}} = \mathbf{b}. \tag{48}$$

The conjugate gradient method can now be applied to any of these two linear systems, leading to the CGNE (acronym for conjugate gradient for the normal equation) method when applied to (47), and to the *minimal error* method[35] when applied to (48). The latter terminology comes from the fact that the underlying algorithm generates a sequence $\{\mathbf{x}^{(k)} = \mathrm{A}^*\mathbf{y}^{(k)}\}$ which minimizes the scalar quantity:

$$\langle \mathbf{r}, (\mathrm{A}\mathrm{A}^*)^{-1}\mathbf{r}\rangle_{\mathbb{C}} = \|\hat{\mathbf{x}} - \mathbf{x}\|^2_{\mathbb{C}},$$

where $\mathbf{x} = \mathrm{A}^*\mathbf{y}$ and $\mathbf{r} = \mathbf{b} - \mathrm{A}\mathrm{A}^*\mathbf{y}$, where $\langle\cdot,\cdot\rangle_{\mathbb{C}}$ denotes the complex inner-product defined on $\mathbb{C}^K$, and where $\|\cdot\|_{\mathbb{C}}$ denotes the norm induced by $\langle\cdot,\cdot\rangle_{\mathbb{C}}$. For both methods, the convergence of $\{\mathbf{x}^{(k)}\}$ towards the solution $\hat{\mathbf{x}}$ of (46) is guaranteed since $\mathrm{A}\mathrm{A}^*$ and $\mathrm{A}^*\mathrm{A}$ are hermitian positive definite matrices. The main drawback of these two methods is that, by changing the original linear system (46) to one of the two equivalent systems, (47) or (48), the conditioning number has been deteriorated and iterations will converge very slowly. The slowdown of the algorithm is all the more important as the grid mesh sizes, $\Delta\theta$ and $\Delta\xi = \max\{\Delta\xi_{\mathrm{w}}, \Delta\xi_{\mathrm{s}}, \Delta\xi_{\mathrm{a}}\}$, get smaller (or as M and N have increasing values). Notwithstanding, a mesh convergence test in depth and in azimuth remains important. Therefore, in order to improve the conditioning of the iteration matrix, we first multiply (46) by a preconditioning matrix Q^{-1}:

$$\mathrm{Q}^{-1}\mathrm{A}\hat{\mathbf{x}} = \mathrm{Q}^{-1}\mathbf{b}. \tag{49}$$

Then, by letting $\hat{\mathbf{x}} = (\mathrm{Q}^{-1}\mathrm{A})^* \hat{\mathbf{y}}$, we obtain:

$$(\mathrm{Q}^{-1}\mathrm{A})(\mathrm{Q}^{-1}\mathrm{A})^* \hat{\mathbf{y}} = \mathrm{Q}^{-1}\mathbf{b}. \tag{50}$$

Again, the conjugate gradient method can be applied to solve (50) and the convergence of the algorithm is guaranteed due to the positive definite hermitian property of matrix $(\mathrm{Q}^{-1}\mathrm{A})(\mathrm{Q}^{-1}\mathrm{A})^*$. A loop of the iterative algorithm involves 7 steps:

$$\begin{aligned}
&\zeta^{(k)} = \|\mathbf{g}^{(k)}\|^2_{\mathbb{C}}/\|\mathbf{p}^{(k)}\|^2_{\mathbb{C}}\\
&\mathbf{x}^{(k+1)} = \mathbf{x}^{(k)} + \zeta^{(k)}\mathbf{p}^{(k)}\\
&\mathbf{r}^{(k+1)} = \mathbf{r}^{(k)} - \zeta^{(k)}\mathrm{A}\mathbf{p}^{(k)}\\
&\mathrm{Q}\mathbf{g}^{(k+1)} = \mathbf{r}^{(k+1)}\\
&\kappa^{(k)} = \|\mathbf{g}^{(k+1)}\|^2_{\mathbb{C}}/\|\mathbf{g}^{(k)}\|^2_{\mathbb{C}}\\
&\mathrm{Q}^*\mathbf{q}^{(k+1)} = \mathbf{g}^{(k+1)}\\
&\mathbf{p}^{(k+1)} = \mathrm{A}^*\mathbf{q}^{(k+1)} + \kappa^{(k)}\mathbf{p}^{(k)}
\end{aligned}$$

where the initial vector $\mathbf{x}^{(0)}$ is chosen arbitrarily, $\mathbf{r}^{(0)} = \mathbf{b} - \mathrm{A}\mathbf{x}^{(0)}$, and where vectors $\mathbf{g}^{(0)}$, $\mathbf{q}^{(0)}$, $\mathbf{p}^{(0)}$ satisfy $\mathrm{Q}\mathbf{g}^{(0)} = \mathbf{r}^{(0)}$, $\mathrm{Q}^*\mathbf{q}^{(0)} = \mathbf{g}^{(0)}$ and $\mathbf{p}^{(0)} = \mathrm{A}^*\mathbf{q}^{(0)}$. The loop is repeated until the relative residual norm, $\|\mathbf{r}^{(k)}\|_{\mathbb{C}}/\|\mathbf{b}\|_{\mathbb{C}}$, is less than a given precision (tolerance) ϵ. Each loop requires solving two auxiliary linear systems ($\mathrm{Q}\mathbf{g}^{(k+1)} = \mathbf{r}^{(k+1)}$ and $\mathrm{Q}^*\mathbf{q}^{(k+1)} = \mathbf{g}^{(k+1)}$) involving the preconditioning matrix Q and its adjoint Q^*. The efficiency of the solver highly depends on the preconditioning procedure. Adapting the preconditioning approach used by Bayliss *et al.*[36] we construct a preconditioner using the tridiagonal matrix derived from the $\mathrm{M} \times 2\mathrm{D}$ associated model (M sections in the azimuthal direction):

$$\mathrm{Q} = \mathrm{I} + \mathrm{i}\frac{\Delta r}{2}\tilde{\mathrm{T}}^{\ell+\frac{1}{2}}.$$

A re-ordering of the unknowns corresponding to numbering along ξ at constant azimuth leads to the following linear systems:

$$\mathrm{Q}'\mathbf{g}'^{(k+1)} = \mathbf{r}'^{(k+1)} \quad \text{and} \quad \mathrm{Q}'^*\mathbf{q}'^{(k+1)} = \mathbf{g}'^{(k+1)}$$

where $\mathrm{Q}' = \mathrm{P}^T\mathrm{QP}$, with P the permutation matrix which gives the correspondance between a numbering along θ at constant depth and a numbering along ξ at constant azimuth, and where $\mathbf{g}'^{(k+1)} = \mathrm{P}^T\mathbf{g}^{(k+1)}$, $\mathbf{r}'^{(k+1)} = \mathrm{P}^T\mathbf{r}^{(k+1)}$. Any system involving matrix Q' or its adjoint can now be easily inverted since Q' has a block-diagonal structure:

$$\mathrm{Q}' = \begin{pmatrix} \mathrm{Q}'_{(1,1)} & & & \\ & \mathrm{Q}'_{(2,2)} & & \\ & & \ddots & \\ & & & \mathrm{Q}'_{(M,M)} \end{pmatrix}. \tag{51}$$

Indeed, each inversion of Q' is equivalent to the inversion of M (auxiliary) linear systems of order N. Since each block is a square tridiagonal matrix of order N, these inversions can be performed using a fast and robust Gaussian (direct) algorithm optimized for tridiagonal matrices. The amount of storage required depends linearly on the number of grid points. In addition, few vectors need to be stored. Hence the storage is much less than that required by any version of the Gaussian elimination. As will be shown in the next section, practical numerical results demonstrate that the acceleration due to the preconditioning is so large compared to the non-preconditioning iterative method that the additional operations inherent to the preconditioning procedure are negligible.

5. Numerical Simulations

To assess the efficiency of the newly developed 3D narrow-angle PE model based on the change-of-variable technique presented in the previous section, we consider a three-dimensional extension of the original two-dimensional penetrable wedge-shaped problem originally proposed as an ASA benchmark in 1987, and extensively used to analyze accuracy and efficiency of various two-dimensional ocean acoustics models and later extended to a full 3D benchmark case by Fawcett.[9] Except when specified explicitly otherwise, all the 2D and 3D numerical results presented hereafter have been obtained running the new change-of-variable technique based code. The numerical simulations have been performed on a 2.8 GHz mono-processor workstation with a 2 GB memory. We consider an isovelocity water layer of density $\rho_\mathrm{w} = 1\,\mathrm{g/cm^3}$ and sound speed $c_\mathrm{w} = 1500\,\mathrm{m/s}$, overlying a lossy homogeneous halfspace sedimental layer of density $\rho_\mathrm{s} = 1.5\,\mathrm{g/cm^3}$, sound speed $c_\mathrm{s} = 1700\,\mathrm{m/s}$ and attenuation $\alpha_\mathrm{s} = 0.5\,\mathrm{dB}/\lambda$, which leads to a critical grazing angle value of approximately 28 deg. No shear energy is assumed in the sediment. The surface parametrization of the water-sediment interface Σ_sed is given by:

$$s(r,\theta) = 200(1 - r\cos\theta/4000), \tag{52}$$

leading to a 2.86 deg-upslope at $\theta = 0°$, a 2.86 deg-downslope at $\theta = 180°$, and a zero-slope at both $\theta = 90°$ and $\theta = 270°$ which we will refer to as cross-slope directions. Note that for directions perpendicular to the wedge apex (i.e. for both $\theta = 0°$ and $\theta = 180°$), the cylindrical symmetry assumption is locally valid and no (or at least weak) horizontal refraction of the propagating sound is expected for adjacent azimuthal angles. We thus focus on the cross-slope direction, where larger 3D effects occur. A cw point source emitting at

25 Hz is placed at a depth of 100 m. It leads to the existence of three propagating modes at the source location. We consider propagation ranges greater than the present range handled by Eq. (52), i.e. 4 km. Hence, for numerical purposes, the interface depth is truncated at a minimum depth of 5 m and at a maximum depth of 395 m. We display in Fig. 3

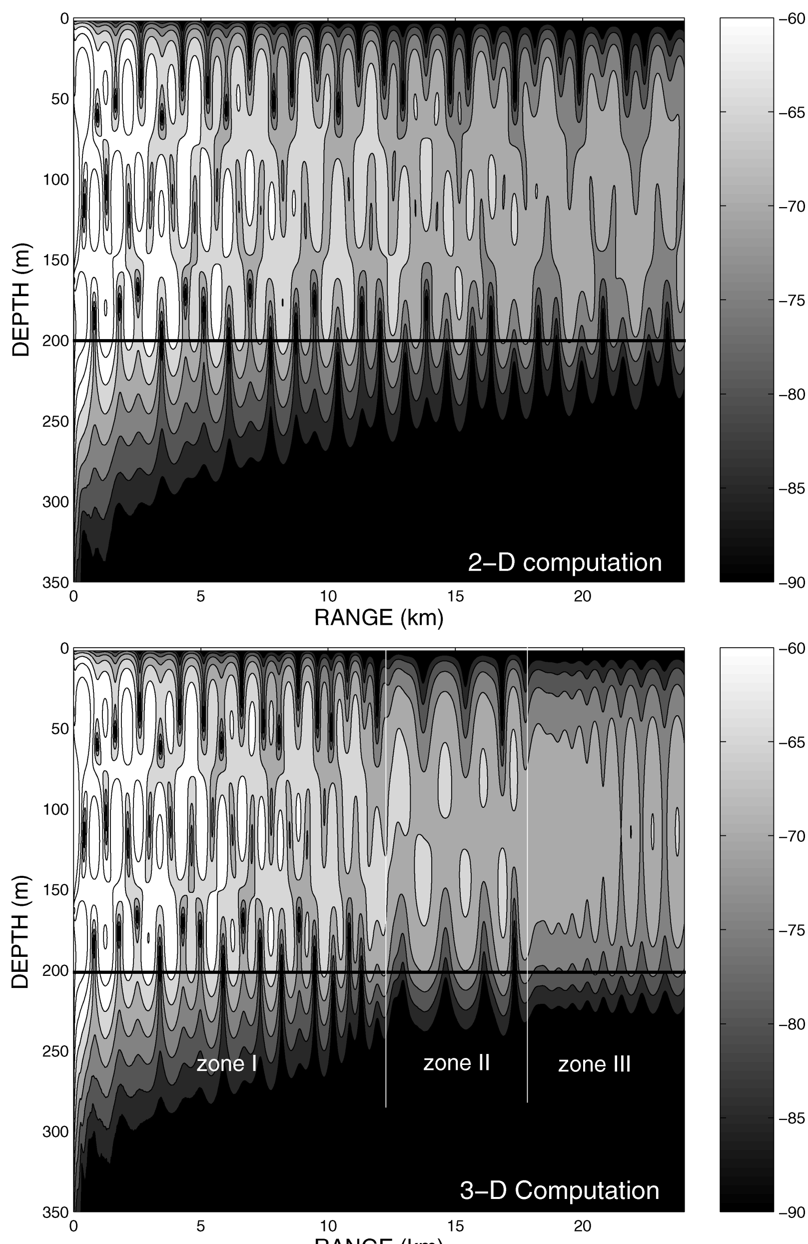

Fig. 3. Transmission loss (vertical slices at constant azimuth $\theta = 90^\circ$, across-slope) corresponding to 2D (upper subplot) and 3D (lower subplot) narrow-angle PE computations.

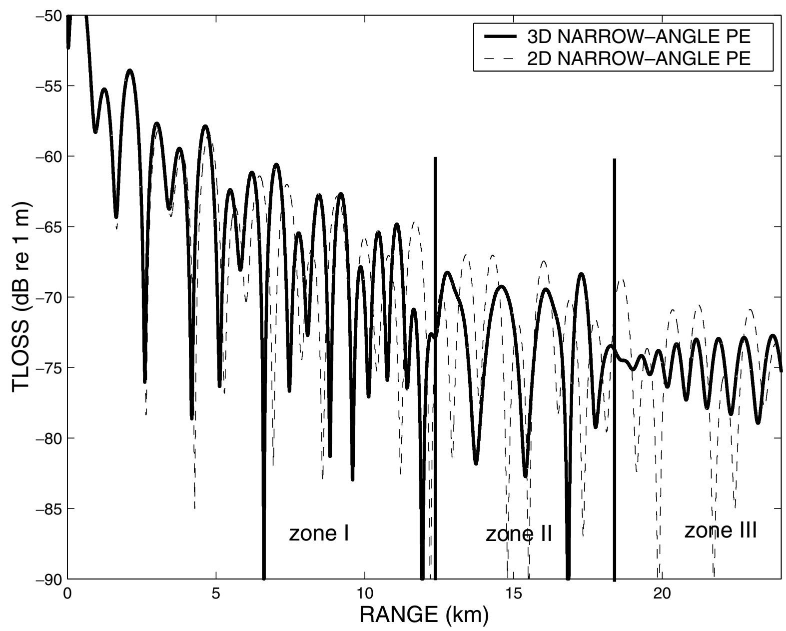

Fig. 4. Transmission loss (in dB re 1 m) curves at a receiver depth of 30 m in the cross-slope direction $\theta = 90^\circ$ corresponding to 2D (dashed line) and 3D (bold solid line) narrow-angle PE computations.

gray-scale images of the transmission loss (vertical slices, $\theta = 90^\circ$) corresponding to 2D (upper subplot) and 3D (lower subplot) PE computations. We also display in Fig. 4 TL-versus-range curves (in dB re 1 m) corresponding to the cross-slope direction ($\theta = 90^\circ$) and to a receiver depth of 30 m. The 2D and 3D solutions are shown in dashed line and bold solid line respectively. The maximum computation range is 24 km. The azimuth- and range-dependent transformation of the depth coordinate has been performed using Eq. (18) with $s_* = 200$ m, which corresponds to the water depth at the source location. To simulate a bottom halfspace, we have used an artificial absorbing bottom layer with a ξ-dependent attenuation coefficient $\alpha_{\rm a} = \alpha_{\rm s} + 0.05 \times (\xi - z_{\rm abs})$, this absorbing layer starting at $\xi = 500$ m and ending at $\xi = 600$ m, with density and sound speed values identical to the ones used in the sediment. The 2D and 3D algorithms have been initialized at $r = 0$ using a modal starter. The source field has been assumed to be omnidirectional and we have used $c_0 = 1500$ m/s. Since long range propagation is considered, the initial field includes only the three propagating modes existing at the source location. As expected, the 2D field exhibits the interference pattern of the three (initially present) propagating modes for all ranges. The differences between the 2D and 3D solutions are very weak in the vicinity of the source, but become more and more pronounced as the propagation range increases. The 3D effects have been explained in detail by several authors and correspond to intramodal interference effects, leading to the succession of three zones across-slope, with three propagating modes present in zone I, two propagating modes in zone II, and only one propagating mode interfering with itself in zone III.

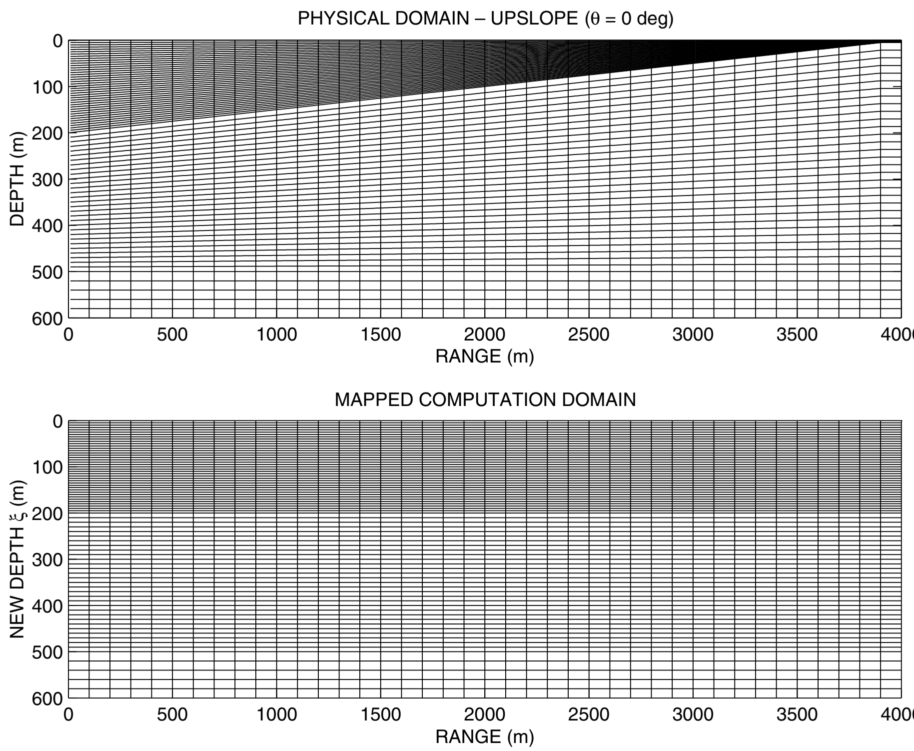

Fig. 5. Mesh grid used in the mapped-computation domain (lower subplot) and its corresponding range-dependent mesh grid in the real physical domain in the upslope direction (upper subplot). For better clarity, only 40 out of the 100 points are represented in depth for the water (first) layer. Likewise, 30 out of the 75 points in the sediment (second layer) are shown. All points belonging to the artificial absorbing (last) layer are represented.

Both 2D and 3D computations have been carried out using $\Delta r = 10\,\mathrm{m}$, $\Delta\xi_{\mathrm{w}} = 2\,\mathrm{m}$, $\Delta\xi_{\mathrm{s}} = 4\,\mathrm{m}$, and $\Delta\xi_{\mathrm{a}} = 20\,\mathrm{m}$ in the mapped computation domain, which corresponds to using $N = 179$ discrete points in depth. It should be noted that among these points, only the 5 last ones lie in the artificial absorbing layer. A vertical slice (which is independent of the azimuthal angle) of the mesh grid used in the mapped computation domain is plotted in Fig. 5 (lower subplot). In particular, a vertical slice in the upslope-direction ($\theta = 0°$) of the corresponding mesh grid in the physical domain is also plotted in Fig. 5 (upper subplot). To show the performance of the nonstationary iterative algorithm presented in Sec. 4.2, we now analyze the number of iterations required for convergence of the algorithm at the specific discrete range $r = 1000\,\mathrm{m}$. By convergence, we mean that the relative residual norm[b] be less than a given precision ϵ supplied by the user. In practice, $\epsilon = 10^{-5}$ is sufficient to get stable results. In Table 1 the number of iterations required for convergence is shown for different values of Δr and for fixed values of the depth and azimuthal increments.

[b]This quantity being naturally produced by the implementation of the iterative algorithm.

Table 1. Iteration results for $\Delta\xi_{\rm w} = 2\,$m, $\Delta\xi_{\rm s} = 4\,$m, $\Delta\xi_{\rm a} = 20\,$m (i.e., $N = 179$), $M = 1440$, $r = 1000\,$m.

	$\epsilon = 10^{-5}$ Number of Iterations		$\epsilon = 10^{-7}$ Number of Iterations		$\epsilon = 10^{-9}$ Number of Iterations	
Δr	Precond.	Unprecond.	Precond.	Unprecond.	Precond.	Unprecond.
20.0 m	13	625	21	850	27	1074
10.0 m	8	308	12	419	15	530
5.0 m	5	148	7	203	8	258
1.0 m	2	24	3	35	3	45
0.5 m	2	10	2	15	3	21

Table 2. Iteration results for $\Delta r = 10\,$m, $M = 1440$, $r = 1000\,$m.

				$\epsilon = 10^{-5}$ Number of Iterations		$\epsilon = 10^{-7}$ Number of Iterations	
$\Delta\xi_{\rm w}$	$\Delta\xi_{\rm s}$	$\Delta\xi_{\rm a}$	N	Precond.	Unprecond.	Precond.	Unprecond.
4.0 m	10 m	50 m	81	7	91	11	127
2.0 m	4 m	20 m	179	8	308	12	419
1.0 m	2 m	10 m	359	11	1148	14	1560
0.5 m	1 m	5 m	719	14	4384	19	6008

In Table 2 the iteration results are given for different combinations of $\Delta\xi_{\rm w}$, $\Delta\xi_{\rm s}$, $\Delta\xi_{\rm a}$, and for fixed values of the azimuthal and range increments. As expected, reducing the size of the range increment, Δr, permits an acceleration of both the preconditioned and unpreconditioned algorithms. On the other hand, reducing the depth increments, $\Delta\xi_{\rm w}$, $\Delta\xi_{\rm s}$, $\Delta\xi_{\rm a}$ (or equivalently increasing N) leads to a degradation of both algorithms. Note however that the degradation of the unpreconditioned algorithm is more rapid than that of the preconditioned one. Despite this degradation, the relative efficiency of the preconditioning strategy is evident. Performances of both iterative algorithms highly also depend on the size of the azimuthal increment $\Delta\theta$. For instance, the number of iterations required for convergence is shown in Table 3 for different values of $\Delta\theta$ and for fixed values of the range and depth increments. In concordance with what has been observed with the depth

Table 3. Iteration results for $\Delta\xi_{\rm w} = 2\,$m, $\Delta\xi_{\rm s} = 4\,$m, $\Delta\xi_{\rm a} = 20\,$m (i.e. $N = 179$), $\Delta r = 10\,$m, $r = 1000\,$m.

	$\epsilon = 10^{-5}$ Number of Iterations		$\epsilon = 10^{-7}$ Number of Iterations	
M	Precond.	Unprecond.	Precond.	Unprecond.
360	2	278	3	379
720	2	284	3	386
1440	8	308	12	419
2880	31	403	47	549
5760	486	816	693	1102

increments, reducing $\Delta\theta$ (or equivalently increasing M) deteriorates the convergence of both the preconditioned and unpreconditioned algorithms. It is also apparent in Table 3 that the preconditioning strategy offers a very poor advantage for large values of M. Numerous simulations have shown that this deterioration is all the more important as the value of the discrete range at which the matrix inversion is performed tends to zero (results not shown here). In fact, both iterative algorithms are very sensitive to the value of the arclength increment Δs defined by:

$$\Delta s = r\Delta\theta = 2\pi r/M,$$

where $\Delta\theta$ is expressed in radians. Therefore, in order to bypass the problem of convergence encountered when computing at small ranges with large values of M, we have chosen to adapt the size of $\Delta\theta$ during the propagation. Unlike N, the number of points used in azimuth is hence not constant in range. The number of azimuthal points has been selected such that the corresponding arclength increment Δs be less than a given fraction of λ, i.e. such that:

$$\Delta s \leq \lambda/\tau \tag{53}$$

for a given (fixed) τ. Since Δs is also function of the r-variable, this means that the integer M should be increased at each step in range, leading to an interpolation procedure between values of the numerical solution on two successive azimuthal grids. In order not to deteriorate the quality of the discretization, the interpolation is achieved at only specific discrete ranges. The strategy is the following: The 3D computation is launched at $r \approx 0$ using $M = 360$ points in azimuth, this number of points being maintained in range until the criterion given by Eq. (53) is no longer satisfied. The number of azimuthal points is then doubled

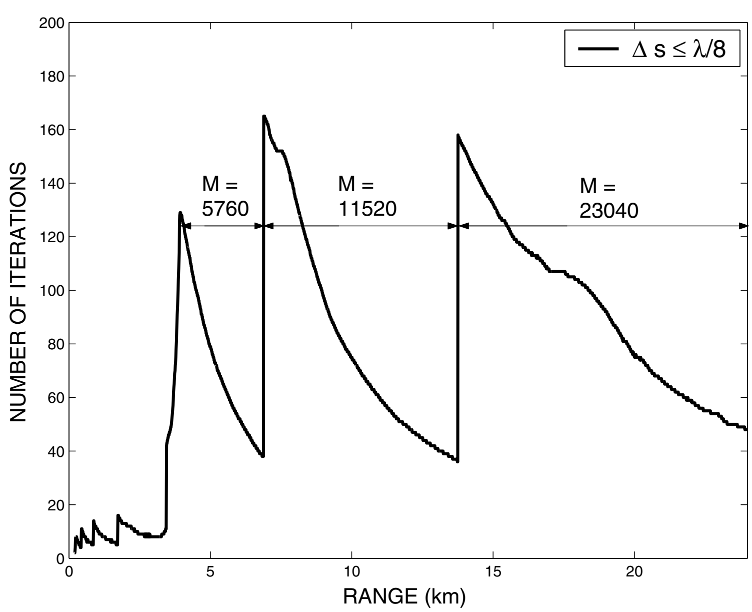

Fig. 6. Iteration results as a function of range for the preconditioned iterative algorithm and $\tau = 8$.

($M = 720$), an interpolation procedure being applied to construct the solution on a 720-point azimuthal grid. The procedure of doubling M at any discrete range for which the criteria given by Eq. (53) is in default is then repeated until the maximum propagation range is reached. Usually, a convergence test with respect to the azimuth consists in running the code with successively decreasing values of $\Delta\theta$ (or equivalently increasing values of M) until the solution starts to stabilize. Here, the convergence test with respect to the azimuth has been handled by running the code with successively increasing values of τ. It has been found that using $\tau = 8$ (i.e. imposing $\Delta s \leq \lambda/8$) is necessary to reach convergence. To this value of τ corresponds a number of azimuthal points equal to $M = 360$ for $r \leq 440\,\mathrm{m}$, $M = 720$ for $440\,\mathrm{m} \leq r \leq 870\,\mathrm{m}$, $M = 1440$ for $870\,\mathrm{m} \leq r \leq 1730\,\mathrm{m}$, $M = 2880$ for $1730\,\mathrm{m} \leq r \leq 3450\,\mathrm{m}$, $M = 5760$ for $3450\,\mathrm{m} \leq r \leq 6890\,\mathrm{m}$, $M = 11520$ for $6890\,\mathrm{m} \leq r \leq 13760\,\mathrm{m}$, and $M = 23040$ for $13760\,\mathrm{m} \leq r \leq r_{\max} = 24000\,\mathrm{m}$.

The number of iterations required for convergence of the preconditioned iterative algorithm is represented as a function of r in Fig. 6 for $\tau = 8$. We display in Fig. 7 TL-versus-range curves corresponding to $\tau = 1/4$, $\tau = 1/2$, $\tau = 1$, $\tau = 2$, $\tau = 4$, and $\tau = 6$. For comparison, we also display the curve corresponding to $\tau = 8$. All the curves of Fig. 7 correspond to the cross-slope direction and to a receiver depth of 30 m. When looking at first sight, we observed that the main 3D effects are reasonably detected using an azimuthal increment $\Delta\theta$ corresponding to $\lambda/2$. This confirms the observation made in Refs. 26 and 27. However, a better description of the 3D effects is obtained with a larger τ, i.e. by using a more stringent criterion. The solution obtained with $\tau = 6$ is very close to the converged solution. Using a criterion $\Delta s \leq \lambda/\tau$ with $\tau < 2$ provides inaccurate 3D solutions.

The narrow-angle 3D PE solution has been compared with a reference numerical solution based on the image source method.[37] The two solutions are plotted in Fig. 8. The bold solid curve corresponds to the narrow-angle 3D PE solution and the dashed curve to the image solution. The two numerical solutions exhibit qualitatively the same three-dimensional effects. Both models lead to a succession of three clearly distinguishable zones across-slope. However, the outsets of zones II and III are shifted by a few kilometers. The two solutions are hence shifted in phase over the entire propagation range. We believe that these differences can be attributed to the three-dimensional narrow-angle approximation used in the 3D PE model since, as shown in Ref. 29, the use a wider-angle approximation in both depth and azimuth permits a better agreement between the parabolic equation and the image solutions.

Comparisons with an other 3D PE model that uses a stair-step technique have been performed. The original three-dimensional parabolic equation based code developed by Fawcett[9] has been used. This 3D PE code uses FFTs to model its azimuthal operator. In order to make some meaningful comparisons, its wide-angle capability (in depth) has been intentionally reduced to narrow-angle. We have run the code using 512, 1024, 2048 and 4096 points in azimuth. Recall that in order to take advantage of the FFT algorithm, the number of azimuthal FFT components must be an integer power of 2. Convergence has been achieved with 4096 points in azimuth. No significant variation has been observed for a smaller azimuthal increment. We plot in Fig. 9 TL-versus-range curves obtained with both

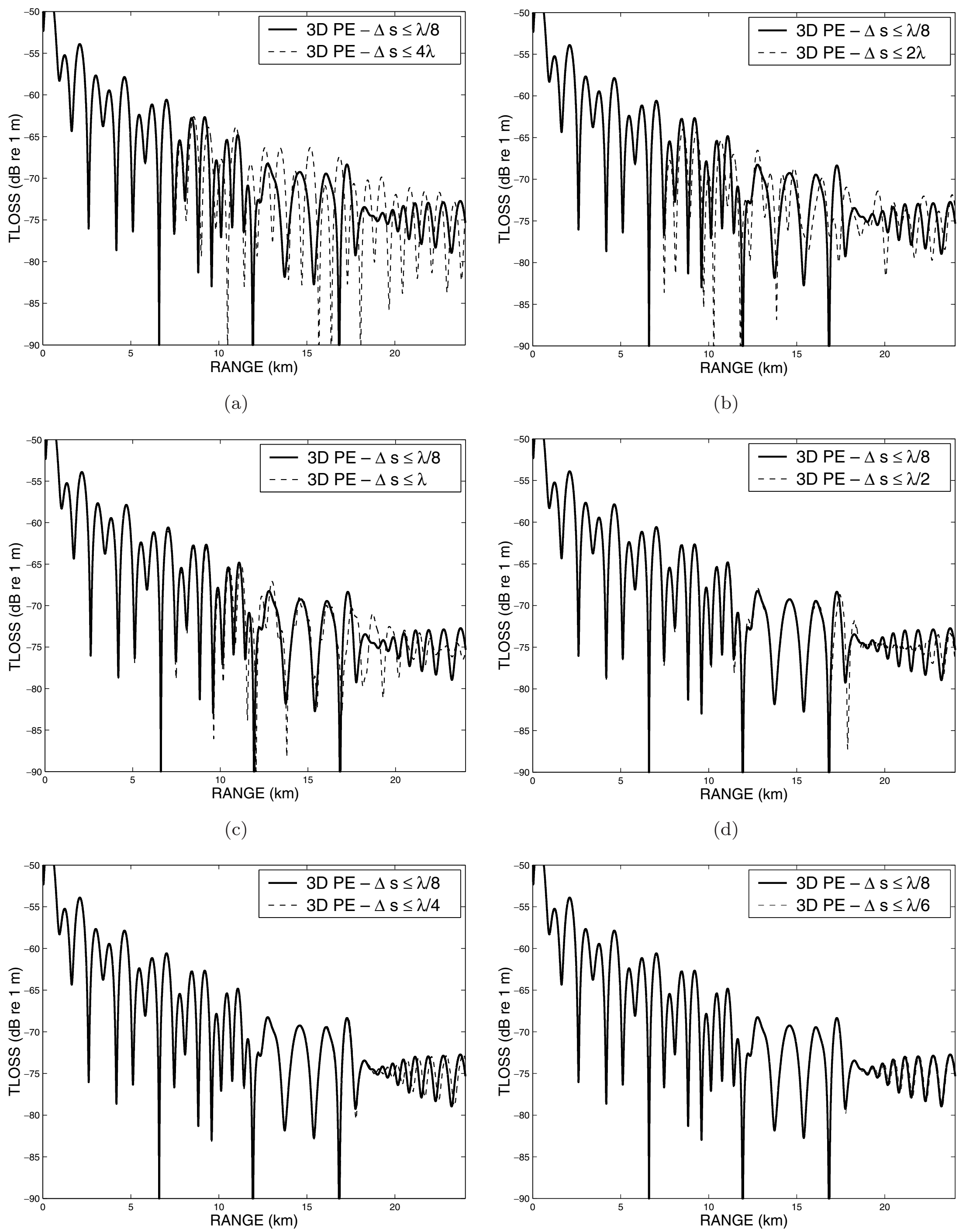

Fig. 7. 3D transmission loss curves (dashed line) at a receiver depth of 30 m and $\theta = 90^\circ$ obtained with 3D computations satisfying the criteria (a) $\Delta s \leq 4\lambda$, (b) $\Delta s \leq 2\lambda$, (c) $\Delta s \leq \lambda$, (d) $\Delta s \leq \lambda/2$, (e) $\Delta s \leq \lambda/4$, (f) $\Delta s \leq \lambda/6$. For each subplot, the curve corresponding to $\Delta s \leq \lambda/8$ has been added (bold solid line) for comparison.

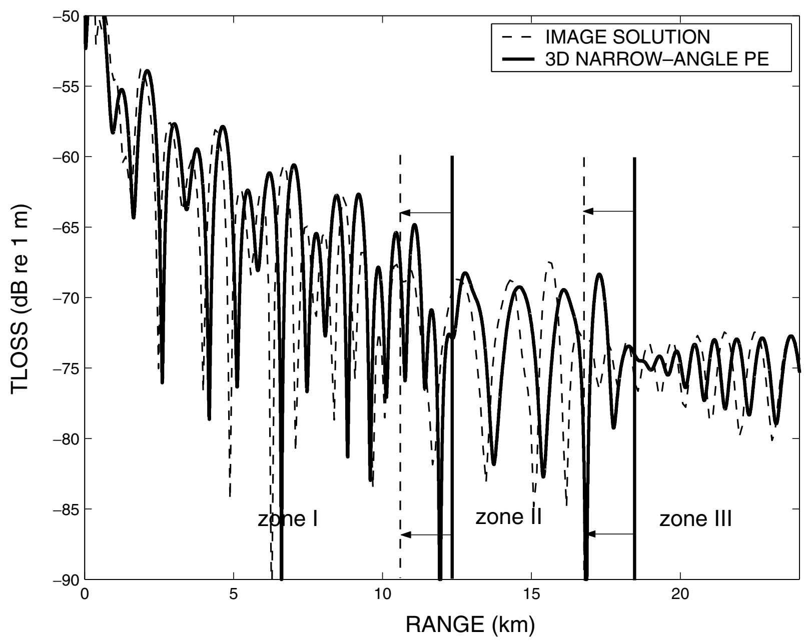

Fig. 8. 3D Transmission loss (in dB re 1 m) comparisons at 25 Hz at a receiver depth of 30 m and across-slope ($\theta = 90°$). The bold solid curve corresponds to the narrow-angle 3D PE solution and the dashed curve to the image solution.

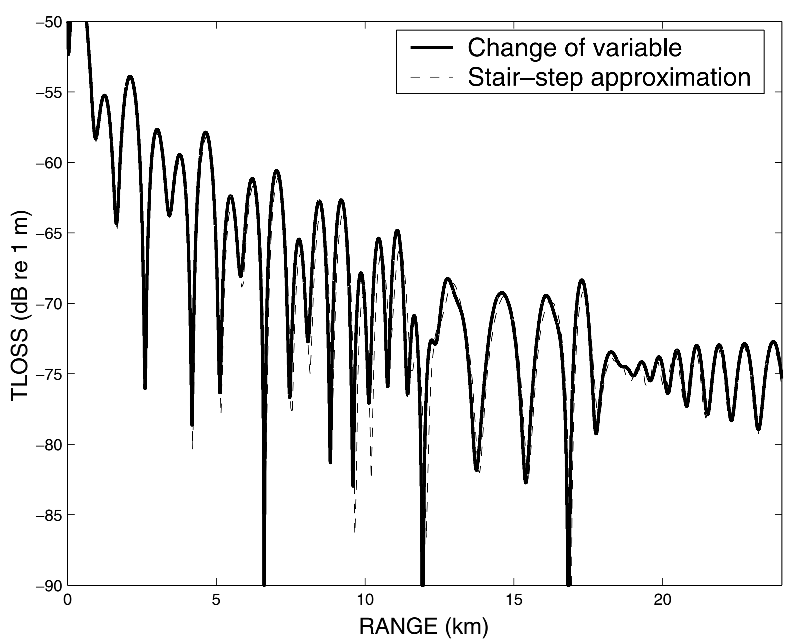

Fig. 9. 3D Transmission loss (in dB re 1 m) comparisons at 25 Hz at a receiver depth of 30 m and across-slope ($\theta = 90°$). Both curves correspond to 3D narrow-angle PE solutions. The solution obtained with the change-of-variable technique is represented in solid line. The solution obtained with the staircase approximation is represented in dashed line.

3D PE models. We observe a quite good agreement of the two solutions, though a shift in phase and in amplitude is present at some ranges. Note that this shift is relatively small in comparison with the shift observed in Refs. 26 and 27 while using the TRIPARADIM code. The only difference between the two models used here is the manner in which they treat the 3D varying bottoms. For the dashed curve, the water-sediment interface is assumed to be locally horizontal at each step in range, the solution satisfying the "flat bottom" condition given by Eq. (14) across the water-sediment interface. For the solid curve, the change-of-variable technique allows an accurate description of the sloping bottom, the solution satisfying the "parabolized" sloping interface condition given by Eq. (11). All the other parameters are identical. For instance, they both consider an horizontal artificial absorbing layer starting at a depth of 500 m and a pressure-release bottom at a depth of 600 m, which was not the case in Refs. 26 and 27.

6. Summary and Discussion

In this paper, a new 3D narrow-angle PE model that treats the interface scattering very accurately has been presented. First, using the same approach as in other works,[25,32] the normal derivative transmission condition at the water-sediment sloping interface has been replaced by a parabolized condition tightly following the paraxial approximation made on the Helmholtz equation, the underlying mathematical model thus satisfying correct energy properties. Second, in order to handle 3D varying geometries, a new change of variable has been used. No stair-step approximation technique has been required. The main advantage of the new change-of-variable technique is that it does not require any homotheticity sedimental layer as in previous work. The parabolized interface conditions have then been incorporated into a finite-element discretization. Numerical simulations have been done on the well-known 3D wedge problem. The solutions exhibit typical 3D effects not predicted by 2D and/or pseudo-3D codes. As expected, the three-dimensional effects are significant across-slope and, in terms of modal energy, regions of modal shadow zones and modal self-interferences are evident.

Comparisons with a 3D PE code that approximates the sloping interfaces by a sequence of stair steps in each azimuth have been made. The comparisons exhibit good agreement between the two approach though a shift in both phase and amplitude can be observed at some ranges. It is now clear that the differences observed in Refs. 26 and 27 were overestimated. Since the stair-step approximation technique allows for faster numerical marching algorithms, we believe that this approach is preferable and more convenient for solving practical problems in 3D environments. We thus highly recommend it when one wants to localize and/or quantify 3D effects. Otherwise, when benchmarking between research codes, a code which utilizes a change-of-variable technique should be used.

Comparisons with a reference solution based on the image source method have shown that the 3D narrow-angle PE solutions obtained running the new code differ somewhat from the solutions obtained with a 3D PE model using a wider-angle approximation. Obviously the narrow-angle capability is too restrictive and should be extended to a wider-angle one. When attempting to take sloping bottoms into account without assuming any stair-step approximation, one should use appropriate parabolized boundary conditions consistent with the wide-angle capability of the parabolic equation based model. Hence, the parabolized boundary conditions used in this paper being consistent only with a narrow-angle paraxial approximation, they should also be extended to wider-angle parabolized boundary conditions. This is currently under way.

The second main drawback is that the use of a transformation of the coordinate system does not allow the splitting of the resulting operator into a depth and azimuthal operator as in other approaches. Instead, a large system of equations in depth and azimuth must be solved at each range step. Though the resulting linear systems are sparse and can be solved using an efficient preconditioning technique, the CPU times are still prohibitive compared to other 3D PE models that are amenable to alternating direction methods. Our aim in this paper was to analyze the influence of the stair-step approximation technique, common to most 3D PE models, on a one-way sound wave propagation problem. We intentionally did not focus on CPU time considerations (although we are convinced of their importances). Acceleration of the convergence of the iterative algorithm should be improved and other iterative solvers like the QMR[38] and GMRES[39] methods should be implemented and tested. It should be noted that the use of the preconditioner is especially attractive for massively parallel computers since, during each iteration, a large number of tridiagonal systems must be solved simultaneously. It could be implemented on a variety of parallel architectures in a straightforward way.

Acknowledgments

This work has been supported by the Greek-French Co-operation Platon Programme 2003/2004. The authors express their thanks to Dr. Georgios E. Zouraris and to Professor Vassilios A. Dougalis for their valuable advices and many fruitful discussion related to this paper. The first author is very grateful to John Fawcett for his many comments concerning 3D PE computations during the early stages of this research work.

Appendix

Let $0 \le \ell \le L-1$. For $1 \le n \le N$, $n \ne n'$, $n \ne n''$, the blocks $\tilde{\mathrm{T}}^{\ell+\frac{1}{2}}_{(n,n-1)}$, $\tilde{\mathrm{T}}^{\ell+\frac{1}{2}}_{(n,n)}$, $\tilde{\mathrm{T}}^{\ell+\frac{1}{2}}_{(n,n+1)}$ are diagonal matrices of order M, whose components are given by:

$$(\tilde{\mathrm{T}}^{\ell+\frac{1}{2}}_{(n,n-1)})_{m,m} = -\frac{(\alpha_\star)_m^{\ell+\frac{1}{2}}}{2k_0(\Delta\xi_\star)^2} - \frac{\mathrm{i}(\partial_r s)_m^{\ell+\frac{1}{2}}}{2\Delta\xi_\star}\left(\frac{(\mu_\star)_{m,n-1}^{\ell+\frac{1}{2}} + (\mu_\star)_{m,n}^{\ell+\frac{1}{2}}}{2}\right),$$

$$(\tilde{\mathrm{T}}^{\ell+\frac{1}{2}}_{(n,n)})_{m,m} = \frac{(\alpha_\star)_m^{\ell+\frac{1}{2}}}{k_0(\Delta\xi_\star)^2} - \left(\frac{k_0}{2}(\tilde{\beta}_\star)_{m,n}^{\ell+\frac{1}{2}} + \frac{\mathrm{i}}{2}((\partial_\xi\mu_\star)(\partial_r s))_m^{\ell+\frac{1}{2}}\right),$$

$$(\tilde{\mathrm{T}}^{\ell+\frac{1}{2}}_{(n,n+1)})_{m,m} = -\frac{(\alpha_\star)_m^{\ell+\frac{1}{2}}}{2k_0(\Delta\xi_\star)^2} + \frac{\mathrm{i}(\partial_r s)_m^{\ell+\frac{1}{2}}}{2\Delta\xi_\star}\left(\frac{(\mu_\star)_{m,n}^{\ell+\frac{1}{2}} + (\mu_\star)_{m,n+1}^{\ell+\frac{1}{2}}}{2}\right),$$

for $1 \leq m \leq M$, where symbol "$\star$" denotes "w" if $1 \leq n < n'$, "s" if $n' < n < n''$, and "a" if $n'' < n \leq N$. For the particular value of n being equal to n', the diagonal components of $\tilde{\mathrm{T}}^{\ell+\frac{1}{2}}_{(n',n'-1)}$, $\tilde{\mathrm{T}}^{\ell+\frac{1}{2}}_{(n',n')}$ and $\tilde{\mathrm{T}}^{\ell+\frac{1}{2}}_{(n',n'+1)}$ write:

$$(\tilde{\mathrm{T}}^{\ell+\frac{1}{2}}_{(n',n'-1)})_{m,m} = \gamma_{\mathrm{s}} \left[-\frac{((\alpha_{\mathrm{w}})(\varepsilon_{\mathrm{w}}))^{\ell+\frac{1}{2}}_m}{2k_0(\Delta\xi_{\mathrm{w}})^2} - \frac{\mathrm{i}((\partial_r s)(\varepsilon_{\mathrm{w}}))^{\ell+\frac{1}{2}}_m}{2\Delta\xi_{\mathrm{w}}} \left(\frac{(\mu_{\mathrm{w}})^{\ell+\frac{1}{2}}_{m,n'-1} + (\mu_{\mathrm{w}})^{\ell+\frac{1}{2}}_{m,n'}}{2} \right) \right],$$

$$(\tilde{\mathrm{T}}^{\ell+\frac{1}{2}}_{(n',n')})_{m,m} = \gamma_{\mathrm{s}} \left[\frac{((\alpha_{\mathrm{w}})(\varepsilon_{\mathrm{w}}))^{\ell+\frac{1}{2}}_m}{2k_0(\Delta\xi_{\mathrm{w}})^2} - \frac{(\varepsilon_{\mathrm{w}})^{\ell+\frac{1}{2}}_m}{2} \left(\frac{k_0}{2}(\tilde{\beta}_{\mathrm{w}})^{\ell+\frac{1}{2}}_{m,n'} + \frac{\mathrm{i}}{2}\left((\partial_\xi \mu_{\mathrm{w}})(\partial_r s)\right)^{\ell+\frac{1}{2}}_m \right) \right]$$
$$+ \gamma_{\mathrm{w}} \left[\frac{((\alpha_{\mathrm{s}})(\varepsilon_{\mathrm{s}}))^{\ell+\frac{1}{2}}_m}{2k_0(\Delta\xi_{\mathrm{s}})^2} - \frac{(\varepsilon_{\mathrm{s}})^{\ell+\frac{1}{2}}_m}{2} \left(\frac{k_0}{2}(\tilde{\beta}_{\mathrm{s}})^{\ell+\frac{1}{2}}_{m,n'} + \frac{\mathrm{i}}{2}((\partial_\xi \mu_{\mathrm{s}})(\partial_r s))^{\ell+\frac{1}{2}}_m \right) \right],$$

$$(\tilde{\mathrm{T}}^{\ell+\frac{1}{2}}_{(n',n'+1)}) = \gamma_{\mathrm{w}} \left[-\frac{((\alpha_{\mathrm{s}})(\varepsilon_{\mathrm{s}}))^{\ell+\frac{1}{2}}_m}{2k_0(\Delta\xi_{\mathrm{s}})^2} + \frac{\mathrm{i}((\partial_r s)(\varepsilon_{\mathrm{s}}))^{\ell+\frac{1}{2}}_m}{2\Delta\xi_{\mathrm{s}}} \left(\frac{(\mu_{\mathrm{s}})^{\ell+\frac{1}{2}}_{m,n'} + (\mu_{\mathrm{s}})^{\ell+\frac{1}{2}}_{m,n'+1}}{2} \right) \right]$$

for $1 \leq m \leq M$, where

$$\gamma_{\mathrm{w}} = \frac{2\rho_{\mathrm{w}}\Delta\xi_{\mathrm{s}}}{\rho_{\mathrm{s}}\Delta\xi_{\mathrm{w}}(\varepsilon_{\mathrm{w}})^{\ell+\frac{1}{2}}_m + \rho_{\mathrm{w}}\Delta\xi_{\mathrm{s}}(\varepsilon_{\mathrm{s}})^{\ell+\frac{1}{2}}_m}, \quad \gamma_{\mathrm{s}} = \frac{2\rho_{\mathrm{s}}\Delta\xi_{\mathrm{w}}}{\rho_{\mathrm{s}}\Delta\xi_{\mathrm{w}}(\varepsilon_{\mathrm{w}})^{\ell+\frac{1}{2}}_m + \rho_{\mathrm{w}}\Delta\xi_{\mathrm{s}}(\varepsilon_{\mathrm{s}})^{\ell+\frac{1}{2}}_m}.$$

For $1 \leq n \leq N$, the blocks $\tilde{\mathrm{S}}^{\ell+\frac{1}{2}}_{(n,n-1)}$, $\tilde{\mathrm{S}}^{\ell+\frac{1}{2}}_{(n,n)}$, $\tilde{\mathrm{S}}^{\ell+\frac{1}{2}}_{(n,n+1)}$ are matrices of order M, mainly tridiagonal:

$$\begin{aligned}
&(\tilde{\mathrm{S}}^{\ell+\frac{1}{2}}_{(n,n-1)})_{m,m-1} = \mu^-_{m,n}, && (\tilde{\mathrm{S}}^{\ell+\frac{1}{2}}_{(n,n-1)})_{m,m} = \vartheta^-_{m,n}, && (\tilde{\mathrm{S}}^{\ell+\frac{1}{2}}_{(n,n-1)})_{m,m+1} = -\mu^+_{m,n},\\
&(\tilde{\mathrm{S}}^{\ell+\frac{1}{2}}_{(n,n)})_{m,m-1} = \kappa^-_{m,n}, && (\tilde{\mathrm{S}}^{\ell+\frac{1}{2}}_{(n,n)})_{m,m} = \vartheta_{m,n}, && (\tilde{\mathrm{S}}^{\ell+\frac{1}{2}}_{(n,n)})_{m,m+1} = \kappa^+_{m,n},\\
&(\tilde{\mathrm{S}}^{\ell+\frac{1}{2}}_{(n,n+1)})_{m,m-1} = -\mu'^-_{m,n}, && (\tilde{\mathrm{S}}^{\ell+\frac{1}{2}}_{(n,n+1)})_{m,m} = \vartheta^+_{m,n}, && (\tilde{\mathrm{S}}^{\ell+\frac{1}{2}}_{(n,n+1)})_{m,m+1} = \mu'^+_{m,n},
\end{aligned}$$

with entries in the upper right and lower left corners:

$$\begin{aligned}
&(\tilde{\mathrm{S}}^{\ell+\frac{1}{2}}_{(n,n-1)})_{1,M} = \mu^-_{1,n}, && (\tilde{\mathrm{S}}^{\ell+\frac{1}{2}}_{(n,n-1)})_{M,1} = -\mu^+_{M,n},\\
&(\tilde{\mathrm{S}}^{\ell+\frac{1}{2}}_{(n,n)})_{1,M} = \kappa^-_{1,n}, && (\tilde{\mathrm{S}}^{\ell+\frac{1}{2}}_{(n,n)})_{M,1} = \kappa^+_{M,n},\\
&(\tilde{\mathrm{S}}^{\ell+\frac{1}{2}}_{(n,n+1)})_{1,M} = -\mu'^-_{1,n}, && (\tilde{\mathrm{S}}^{\ell+\frac{1}{2}}_{(n,n+1)})_{M,1} = \mu'^+_{M,n}.
\end{aligned}$$

The scalars $\mu^{\pm}_{m,n}$, $\mu'^{\pm}_{m,n}$, $\kappa^{\pm}_{m,n}$, $\vartheta^{\pm}_{m,n}$, $\vartheta_{m,n}$, $1 \leq m \leq M$ are given, for all $n \in \{1, \ldots, N\}$, $n \neq n'$, $n \neq n''$, by:

$$\mu^{\pm}_{m,n} = \frac{(\mu_\star)^{\ell+\frac{1}{2}}_{m,n-1}((\partial_\theta s)(\varepsilon_\star))^{\ell+\frac{1}{2}}_{m} + (\mu_\star)^{\ell+\frac{1}{2}}_{m\pm1,n}((\partial_\theta s)(\varepsilon_\star))^{\ell+\frac{1}{2}}_{m\pm1}}{4\Delta\theta\Delta\xi_\star(\varepsilon_\star)^{\ell+\frac{1}{2}}_{m}},$$

$$\mu'^{\pm}_{m,n} = \frac{(\mu_\star)^{\ell+\frac{1}{2}}_{m,n+1}((\partial_\theta s)(\varepsilon_\star))^{\ell+\frac{1}{2}}_{m} + (\mu_\star)^{\ell+\frac{1}{2}}_{m\pm1,n}((\partial_\theta s)(\varepsilon_\star))^{\ell+\frac{1}{2}}_{m\pm1}}{4\Delta\theta\Delta\xi_\star(\varepsilon_\star)^{\ell+\frac{1}{2}}_{m}},$$

$$\kappa^{\pm}_{m,n} = -\left(\frac{(\varepsilon_\star)^{\ell+\frac{1}{2}}_{m\pm1} + (\varepsilon_\star)^{\ell+\frac{1}{2}}_{m}}{2}\right)\frac{1}{(\varepsilon_\star)^{\ell+\frac{1}{2}}_{m}\,\Delta\theta^2},$$

$$\vartheta^{\pm}_{m,n} = -\left(\frac{(\mu^2_\star)^{\ell+\frac{1}{2}}_{m,n\pm1} + (\mu^2_\star)^{\ell+\frac{1}{2}}_{m,n}}{2}\right)\frac{((\partial_\theta s)^2)^{\ell+\frac{1}{2}}_{m}}{(\Delta\xi_\star)^2},$$

$$\begin{aligned}\vartheta_{m,n} = {}&\left(\frac{(\varepsilon_\star)^{\ell+\frac{1}{2}}_{m+1} + 2(\varepsilon_\star)^{\ell+\frac{1}{2}}_{m} + (\varepsilon_\star)^{\ell+\frac{1}{2}}_{m-1}}{2}\right)\frac{1}{(\varepsilon_\star)^{\ell+\frac{1}{2}}_{m}\,\Delta\theta^2}\\ &+\left(\frac{(\mu^2_\star)^{\ell+\frac{1}{2}}_{m,n-1} + 2(\mu^2_\star)^{\ell+\frac{1}{2}}_{m,n} + (\mu^2_\star)^{\ell+\frac{1}{2}}_{m,n+1}}{2}\right)\frac{((\partial_\theta s)^2)^{\ell+\frac{1}{2}}_{m}}{(\Delta\xi_\star)^2}.\end{aligned}$$

In particular for $n = n'$, the scalars $\mu^{\pm}_{m,n'}$, $\mu'^{\pm}_{m,n'}$, $\kappa^{\pm}_{m,n'}$, $\vartheta^{\pm}_{m,n'}$, $\vartheta_{m,n'}$, $1 \leq m \leq M$, are given by:

$$\mu^{\pm}_{m,n'} = \gamma_{\mathrm{s}}\left[\frac{(\mu_{\mathrm{w}})^{\ell+\frac{1}{2}}_{m,n'-1}((\partial_\theta s)(\varepsilon_{\mathrm{w}}))^{\ell+\frac{1}{2}}_{m} + (\mu_{\mathrm{w}})^{\ell+\frac{1}{2}}_{m\pm1,n'}((\partial_\theta s)(\varepsilon_{\mathrm{w}}))^{\ell+\frac{1}{2}}_{m\pm1}}{4\Delta\theta\Delta\xi_{\mathrm{w}}}\right],$$

$$\mu'^{\pm}_{m,n'} = \gamma_{\mathrm{w}}\left[\frac{(\mu_{\mathrm{s}})^{\ell+\frac{1}{2}}_{m,n'+1}((\partial_\theta s)(\varepsilon_{\mathrm{s}}))^{\ell+\frac{1}{2}}_{m} + (\mu_{\mathrm{s}})^{\ell+\frac{1}{2}}_{m\pm1,n'}((\partial_\theta s)(\varepsilon_{\mathrm{s}}))^{\ell+\frac{1}{2}}_{m\pm1}}{4\Delta\theta\Delta\xi_{\mathrm{s}}}\right],$$

$$\begin{aligned}\kappa^{\pm}_{m,n'} = \gamma_{\mathrm{s}}\Bigg[&-\frac{1}{2}\left(\frac{(\varepsilon_{\mathrm{w}})^{\ell+\frac{1}{2}}_{m\pm1} + (\varepsilon_{\mathrm{w}})^{\ell+\frac{1}{2}}_{m}}{2}\right)\frac{1}{\Delta\theta^2}\\ &\pm\frac{(\mu_{\mathrm{w}})^{\ell+\frac{1}{2}}_{m\pm1,n'}((\partial_\theta s)(\varepsilon_{\mathrm{w}}))^{\ell+\frac{1}{2}}_{m\pm1} - (\mu_{\mathrm{w}})^{\ell+\frac{1}{2}}_{m,n'}((\partial_\theta s)(\varepsilon_{\mathrm{w}}))^{\ell+\frac{1}{2}}_{m}}{4\Delta\theta\Delta\xi_{\mathrm{w}}}\Bigg]\end{aligned}$$

$$+ \gamma_{\mathrm{w}} \left[-\frac{1}{2} \left(\frac{(\varepsilon_{\mathrm{s}})_{m\pm1}^{\ell+\frac{1}{2}} + (\varepsilon_{\mathrm{s}})_{m}^{\ell+\frac{1}{2}}}{2} \right) \frac{1}{\Delta\theta^2} \right.$$

$$\left. \pm \frac{(\mu_{\mathrm{s}})_{m,n'}^{\ell+\frac{1}{2}}((\partial_\theta s)(\varepsilon_{\mathrm{s}}))_{m}^{\ell+\frac{1}{2}} - (\mu_{\mathrm{s}})_{m\pm1,n'}^{\ell+\frac{1}{2}}((\partial_\theta s)(\varepsilon_{\mathrm{s}}))_{m\pm1}^{\ell+\frac{1}{2}}}{4\Delta\theta\Delta\xi_{\mathrm{s}}} \right],$$

$$\vartheta_{m,n'}^{-} = \gamma_{\mathrm{s}} \left[-\left(\frac{(\mu_{\mathrm{w}}^2)_{m,n'-1}^{\ell+\frac{1}{2}} + (\mu_{\mathrm{w}}^2)_{m,n'}^{\ell+\frac{1}{2}}}{2} \right) \frac{((\partial_\theta s)^2)(\varepsilon_{\mathrm{w}}))_{m}^{\ell+\frac{1}{2}}}{(\Delta\xi_{\mathrm{w}})^2} \right],$$

$$\vartheta_{m,n'}^{+} = \gamma_{\mathrm{w}} \left[-\left(\frac{(\mu_{\mathrm{s}}^2)_{m,n'+1}^{\ell+\frac{1}{2}} + (\mu_{\mathrm{s}}^2)_{m,n'}^{\ell+\frac{1}{2}}}{2} \right) \frac{((\partial_\theta s)^2)(\varepsilon_{\mathrm{s}}))_{m}^{\ell+\frac{1}{2}}}{(\Delta\xi_{\mathrm{s}})^2} \right],$$

$$\vartheta_{m,n'} = \gamma_{\mathrm{s}} \left[\frac{1}{2} \left(\frac{(\varepsilon_{\mathrm{w}})_{m+1}^{\ell+\frac{1}{2}} + 2(\varepsilon_{\mathrm{w}})_{m}^{\ell+\frac{1}{2}} + (\varepsilon_{\mathrm{w}})_{m-1}^{\ell+\frac{1}{2}}}{2} \right) \frac{1}{\Delta\theta^2} \right.$$

$$\left. + \left(\frac{(\mu_{\mathrm{w}}^2)_{m,n'-1}^{\ell+\frac{1}{2}} + (\mu_{\mathrm{w}}^2)_{m,n'}^{\ell+\frac{1}{2}}}{2} \right) \frac{((\partial_\theta s)^2\,(\varepsilon_{\mathrm{w}}))_{m}^{\ell+\frac{1}{2}}}{(\Delta\xi_{\mathrm{w}})^2} \right]$$

$$\times \gamma_{\mathrm{w}} \left[\frac{1}{2} \left(\frac{(\varepsilon_{\mathrm{s}})_{m+1}^{\ell+\frac{1}{2}} + 2(\varepsilon_{\mathrm{s}})_{m}^{\ell+\frac{1}{2}} + (\varepsilon_{\mathrm{s}})_{m-1}^{\ell+\frac{1}{2}}}{2} \right) \frac{1}{\Delta\theta^2} \right.$$

$$\left. + \left(\frac{(\mu_{\mathrm{s}}^2)_{m,n'+1}^{\ell+\frac{1}{2}} + (\mu_{\mathrm{s}}^2)_{m,n'}^{\ell+\frac{1}{2}}}{2} \right) \frac{((\partial_\theta s)^2\,(\varepsilon_{\mathrm{s}}))_{m}^{\ell+\frac{1}{2}}}{(\Delta\xi_{\mathrm{s}})^2} \right].$$

References

1. D. Lee, A. D. Pierce and E.-C. Shang, Parabolic equation development in the twentieth century, *J. Comp. Acoust.* **8**(4) (2000) 527–637.
2. J. S. Perkins and R. N. Baer, An approximation to the three-dimensional parabolic equation method for acoustic propagation, *J. Acoust. Soc. Am.* **72** (1982) 515–522.
3. R. Doolittle, A. Tolstoy and M. Buckingham, Experimental confirmation of horizontal refraction of CW acoustic radiation from a point source in a wedge-shaped ocean, *J. Acoust. Soc. Am.* **83** (1988) 2117–2125.
4. G. B. Deane, The penetrable wedge as a three-dimensional benchmark, *J. Acoust. Soc. Am.* **103**(6) (1998) 2989.
5. S. A. Glegg, G. B. Deane and I. G. House, Comparison between theory and model scale measurements of the three-dimensional sound propagation in a shear suporting penetrable wedge, *J. Acoust. Soc. Am.* **94**(4) (1993) 2334–2342.
6. A. Tolstoy, 3D propagation issues and models, *J. Comp. Acoust.* **4**(3) (1996) 243–271.
7. R. N. Baer, Propagation through a three-dimensional eddy including effects on an array, *J. Acoust. Soc. Am.* **69** (1981) 70–75.

8. M. D. Collins and S. A. Ching-Bing, A three-dimensional parabolic equation model that includes the effects of rough boundaries, *J. Acoust. Soc. Am.* **87**(3) (1990) 1104–1109.
9. J. A. Fawcett, Modeling three-dimensional propagation in an oceanic wedge using parabolic equation methods, *J. Acoust. Soc. Am.* **93**(5) (1993) 2627–2632.
10. D. Lee, G. Botseas and W. L. Siegmann, Examination of three-dimensionnal effects using a propagation model with azimuth-coupling capability (FOR3D), *J. Acoust. Soc. Am.* **91**(6) (1992) 3192–3202.
11. K. B. Smith, A three-dimensional propagation algorithm using finite azimuthal aperture, *J. Acoust. Soc. Am.* **106**(6) (1999) 3231–3239.
12. C. F. Chen, Y.-T. Lin and D. Lee, A three-dimensional azimuthal wide-angle model, *J. Comp. Acoust.* **7**(4) (1999) 269–288.
13. J. I. Arvelo and A. P. Rosenberg, Three-dimensional effects on sound propagation and matched-field processor, *J. Comp. Acoust.* **9**(1) (2001) 17–39.
14. G. H. Brooke, D. J. Thomson and G. R. Ebbeson, PECan: A Canadian parabolic equation model for underwater sound propagation, *J. Comp. Acoust.* **9** (2001) 69–100.
15. F. Sturm and J. A. Fawcett, On the use of higher-order azimuthal schemes in 3-D PE modelling, *J. Acoust. Soc. Am.* **113**(6) (2003) 3134–3145.
16. M. B. Porter, F. Jensen and C. M. Ferla, The problem of energy-conserving in one-way models, *J. Acoust. Soc. Am.* **89**(3) (1991) 1058–1067.
17. M. D. Collins and E. K. Westwood, A higher order energy-conserving parabolic equation for range-dependent ocean depth, sound speed, and density, *J. Acoust. Soc. Am.* **89**(3) (1991) 1068–1075.
18. M. D. Collins and R. B. Evans, A two way parabolic equation for acoustic backscattering in the ocean, *J. Acoust. Soc. Am.* **91**(3) (1992) 1357–1368.
19. G. H. Brooke and D. J. Thomson, A single-scatter formalism for improving PE calculations in range-dependent media, in *NRL PE WORKSHOP II (Proceedings of the Second Parabolic Equation Workshop)*, eds. S. A. Chin-Bing, D. B. King, J. A. Davies and R. B. Evans (Naval Research Laboratory, 1993), pp. 126–144.
20. G. H. Brooke, D. J. Thomson and P. M. Wort, A sloping boundary condition for efficient PE calculations in range-dependent acoustic media, *J. Comp. Acoust.* **4**(1) (1996) 11–27.
21. N. A. Kampanis and E. T. Flouri, On an energy conserving treatment of variable interfaces in a finite difference PE code, *Acta Acustica united with Acustica* **85** (1999) 18–23.
22. O. A. Godin, Reciprocity and energy conservation within the parabolic approximation, *Wave Motion* **29** (1999) 175–194.
23. D. Mikhin, Energy-conserving and reciprocal solutions for higher-order parabolic equations, *J. Comp. Acoust.* **9**(1) (2001) 183–203.
24. D. Mikhin, Exact discrete nonlocal boundary conditions for high-order Padé parabolic equations, *J. Acoust. Soc. Am.* **116**(5) (2004) 2864–2875.
25. F. Sturm, Modélisation mathématique et numérique d'un problème de propagation en acoustique sous-marine: prise en compte d'un environnement variable tridimensionnel, Ph.D. Thesis, University of Toulon, 1997 (in French).
26. F. Sturm, J. A. Fawcett and F. B. Jensen, Benchmarking two three-dimensional parabolic equation methods, *J. Acoust. Soc. Am.* **103**(5) (1998) 2090:4aUW5.
27. F. Sturm and J. A. Fawcett, Numerical simulation of the effects of the bathymetry on underwater sound propagation using three-dimensional parabolic equation models, *Saclant Memorandum SM-342* (SACLANT Undersea Research Centre, La Spezia, Italy, 1998)
28. F. B. Jensen and C. M. Ferla, Numerical solutions of range-dependent benchmark problems in ocean acoustics, *J. Acoust. Soc. Am.* **87**(4) (1990) 1499–1510.

29. F. Sturm, Numerical study of broadband sound pulse propagation in three-dimensional oceanic waveguides, *J. Acoust. Soc. Am.* **117**(3) (2005) 1058–1079.
30. F. D. Tappert, The parabolic approximation method, in *Wave Propagation and Underwater Acoustics*, eds. J. B. Keller and J. S. Papadakis, Lecture Notes in Physics, Vol. 70 (Springer-Verlag, Heidelberg, 1977), pp. 224–287.
31. W. L. Siegmann, G. A. Kriegsmann and D. Lee, A wide-angle three-dimensional parabolic wave equation, *J. Acoust. Soc. Am.* **78**(2) (1985) 659–664.
32. L. Abrahamsson and H. O. Kreiss, Boundary conditions for the parabolic equation in a range dependent duct, *J. Acoust. Soc. Am.* **87**(6) (1990) 2438–2441.
33. C. Bernardi and M.-C. Pélissier, Spectral approximation of a Schrödinger type equation, *Mathematical Models and Methods in Applied Sciences* **4**(1) (1994) 49–88.
34. V. A. Dougalis and N. A. Kampanis, Finite element methods for the parabolic equation with interface, *J. Comp. Acoust.* **4** (1996) 55–88.
35. M. H. Schultz, D. Lee and K. R. Jackson, Application of the YALE sparse technique to solve the three-dimensional parabolic wave equation, in *Recent Progress in the Development and Application of the Parabolic Equation*, eds. P. D. Scully-Power and D. Lee, Naval Underwater Systems Center Technical Document 7145 (1984).
36. A. Bayliss, C. I. Goldstein and E. Turkel, An iterative method for the Helmholtz equation, *J. Comp. Phys.* **49** (1983) 443–457.
37. E. K. Westwood, Complex ray solutions to the 3D wedge ASA benchmark problems, *J. Acoust. Soc. Am.* **109**(5) (2001) 2333:2aAOa6.
38. R. W. Freund and N. M. Nachtigal, QMR: A quasi-minimal residual method for non-hermitian linear systems, *Numer. Math.* **60** (1991) 315–339.
39. Y. Saad and M. H. Schultz, GMRES: A generalized minimum residual algorithm for solving nonsymmetric linear systems, *J. Sci. Statist. Comput.* **7** (1986) 856–869.